Carbon Trends 10 (2023) 100243

Contents lists available at ScienceDirect

Carbon Trends

journal homepage: www.elsevier.com/locate/cartre

Screening activated carbons produced from recycled petroleum coke for acid gas separation

John H. Jacobs[a], Nancy Chou[a], Kaylan H. McKelvie[a], Jerry A. Commodore[a], Ruohong Sui[a], Kevin L. Lesage[a], Kyle G. Wynnyk[a], Ye Xiao[b], Mark C. Biesinger[c], Josephine M. Hill[b], Robert A. Marriott[a,*]

[a] Department of Chemistry, University of Calgary, 2500 University Drive, N.W., Calgary, AB T2N 1N4, Canada
[b] Department of Chemical and Petroleum Engineering, University of Calgary, 2500 University Drive, N.W., Calgary, AB T2N 1N4, Canada
[c] Surface Science Western, University of Western Ontario, 999 Collip Circle, London, On N6G 0J3, Canada

ARTICLE INFO

Keywords:
H_2S adsorption
Petroleum coke
Activated carbon
Waste material

ABSTRACT

Activated carbons derived from petroleum coke (petcoke) have the potential to (a) help reduce sulfur dioxide emissions through desulfurization, (b) help reduce carbon dioxide and (c) utilize a common waste product. Herein we present results for the selective adsorption of H_2S and CO_2 from a synthetic sour gas mixture using 7 activated carbons, four derived from petcoke and three obtained commercially. The petcoke activated with sodium hydroxide (P_Na) showed an H_2S/CH_4 selectivity up to $S_{H_2S/CH_4} = 152$ in temperature swing adsorption experiments. The H_2S/CH_4 selectivity was observed to be inversely proportional to the BET apparent surface area and directly proportional to the oxygen content of the activated carbons. H_2S/CH_4 and H_2S/CO_2 selectivity for P_Na was found to increase with increasing temperature. The P_Na activated carbon maintained a high H_2S selectivity ($S_{H_2S/CH_4} > 50$ and $S_{H_2S/CO_2} > 20$) after regeneration at temperatures of $T = 423 - 723$ K. Pure component CH_4, CO_2, and H_2S adsorption isotherms at $T = 288.15$ K, 298.15 K and 308.15 K were collected and used to estimate the multi-component adsorption. The results of these studies indicate that the petcoke activated carbons are viable materials for separating H_2S and CO_2 from sour natural gas streams or biogas.

1. Introduction

Hydrogen sulfide (H_2S) is found in natural resources such as sour natural gas, biogas, and sour crude oil, or can be generated through oil upgrading / desulfurization [1]. Aside from the inherent toxicity to humans (immediately dangerous to human life at 100 ppm) [2], H_2S can be corrosive to steel and is also known to poison catalysts (such as those used in fuel cell applications) at concentrations as low as one ppm [3,4]. When left in fuels and combusted, H_2S forms sulfur dioxide (SO_2), which can result in acid rain when emitted into the atmosphere [5,6]. For fuel or sales gas, H_2S and carbon dioxide (CO_2) are removed from the rest of the gas stream before transportation to the end-user.

Petcoke is a by-product of bitumen upgrading and is considered a low-cost waste product. Because it has a high sulfur content, petcoke is unsuitable to be directly used as a fuel or an electrode material, but is promising material for activated carbon (AC) production. Through study of the pure adsorption isotherms, our recent investigation demonstrated that a petcoke AC had the potential for the removal of H_2S and CO_2 from "sour" natural gas [7]. The removal of H_2S from hydrocarbon fluids, also called "gas sweetening" or treatment in the industry, is mostly achieved by selective aqueous alkanolamine absorption of H_2S and CO_2 [8,9]. This technology is known to be expensive and energy-intensive. Among the alternative technologies, pressure swing adsorption processes are promising due to their low carbon footprint, especially using emerging materials with a low cost and high selectivity, such as ACs [8,10–12].

Two noteworthy studies investigated multi-component adsorption on ACs where H_2S was a component [13,14]. Sitthikhankaew et al. [13] investigated H_2S adsorption on a commercial AC, comparing the un-modified AC, steam upgraded AC and a KOH impregnated AC. The authors' objective was to examine how water (H_2O), oxygen (O_2) and CO_2 impacted the adsorption of H_2S on the materials. As such, they used a dynamic breakthrough set-up to carry out their experiments but reported only the changes in H_2S adsorption and did not report the adsorption of the other species. Thus, selectivities for each component could not be calculated. In another study, Zulkefli et al. [14] investigated the adsorption of biogas mixtures onto coconut-shell-derived ACs. The authors investigated the adsorption of H_2S in gas mixtures of H_2S/nitrogen

* Corresponding author.
E-mail address: rob.marriott@ucalgary.ca (R.A. Marriott).

https://doi.org/10.1016/j.cartre.2022.100243
Received 15 August 2022; Received in revised form 22 December 2022; Accepted 28 December 2022

(N_2) and $H_2S/CO_2/N_2$ on both neat and modified ACs. However, the adsorption of the other components was not reported.

From the literature, petcoke has potential as a material for producing ACs [15–18]. Despite the potential of petcoke-derived ACs for H_2S adsorption, only three published articles have reported investigating this subject [7,19,20]. Furthermore, of these three studies, only one presents multi-component data for the adsorption of H_2S [19]. In the work of Li and Chen [19], pure component adsorption isotherms of methane (CH_4), ethane (C_2H_6), propane (C_3H_8), H_2S, CO_2 and N_2 were obtained on an AC derived from petcoke and activated with KOH under N_2 atmosphere at $T = 773$ K. The authors also compared the adsorption of a mixture of the gaseous components previously listed to evaluate the suitability of the AC as a fuel storage material. Although this demonstrated interesting results, the separation performance was not assessed. Mochizuki et al. [20] investigated ammonia (NH_3) and H_2S adsorption on an AC derived from petcoke and activated with KOH under a N_2 atmosphere at $T = 873 – 1073$ K. This study was performed to investigate the effect of surface functionalities and pore structures on the adsorption of NH_3 and H_2S. The authors demonstrated that H_2S adsorption on the petcoke AC was more dependent on the porosity of the ACs rather than on the basic functional groups, whereas NH_3 adsorption was more dependent on the functionality of the ACs. In our previous work [7], pure component adsorption of CO_2, H_2S, CH_4, sulfur dioxide (SO_2), N_2 and oxygen (O_2) was investigated on an AC derived from petcoke and activated with potassium hydroxide (KOH) under a N_2 atmosphere at $T = 1073$ K. Despite the large selection of fluids tested, isotherms were only collected at $T = 298$ K. Thus, further research into the applications of petcoke ACs must be completed.

Pure component adsorption data provides valuable information for the adsorption mechanism and is widely used in modelling multi-component adsorption systems. However, one must approach these estimations cautiously as current multi-component models are often inaccurate with mixtures containing H_2S and should be verified with experimental results. H_2S has a higher polarizability than CO_2 and CH_4 and contains a small permanent dipole moment, thus increasing the interaction with the AC surface. The increased affinity of H_2S to polarizable surfaces often results in poor estimations from models, such as the ideal adsorbed solution theory (IAST) when compared to CH_4 or CO_2 adsorption selectivities [21,22]. De Oliveira et al. investigated CH_4, CO_2, and H_2S adsorption on a coconut-husk-derived AC by collecting pure component isotherms of the sour gas components and then completed selectivity calculations using IAST [23]. This study investigated how temperature and gas composition changed the H_2S/CH_4 and CO_2/CH_4 selectivities; however, validation of the multi-component results has not yet been reported.

In this study, two different multi-component models were assessed to investigate the multi-component adsorption of the petcoke AC. The first model investigated was the competitive Langmuir model (CL). The CL was developed by Markham and Benton in 1931 [24] and has been a popular multi-component model due to its simplicity. The problem with this model is that there is a thermodynamic inconsistency when the capacities of the pure component isotherms are not equivalent. To address this issue, Bai and Yang [25] proposed a multisite CL equation where the differences in capacities of species could be accounted for in a thermodynamically consistent manner. The second model investigated in this work was the IAST model. Myers and Prausnitz first proposed the IAST model in 1965 [26].

There are limited multi-component adsorption studies involving H_2S as a component. Here we present results for the multi-component adsorption of CH_4, CO_2 and H_2S on four different ACs derived from petcoke and three commercial ACs at low- ($p = 2$ bar) and high-pressures ($p = 43$ bar) using an in-house built dynamic breakthrough instrument. The results of the multi-component adsorption experiments are compared to the properties of the ACs as characterized by N_2 physisorption and X-ray photoelectron spectrometry (XPS). Pure component measurements on one of the petcoke ACs are presented and used for multi-component modelling compared to the experimental results.

2. Experimental section

2.1. Materials

Carbon dioxide (CO_2, laser grade, 99.9995%), methane (CH_4, 99.999%), hydrogen sulfide (H_2S 99.6%), nitrogen (N_2, 99.998%) and a simulated acid gas mixture with a helium (He) tracer ($CH_4/CO_2/H_2S$/He, 0.9396:0.0204:0.0003:0.0397) were purchased and used without further purification (Praxair Canada Inc., Mississauga, Ontario, Canada). Gas purities were verified by gas chromatography (GC, TCD/FID and SCD). Water was purified with an in-house EMD Millipore system (18 MΩ·cm). Analytical grade potassium hydroxide (KOH, 85%) was purchased (Alfa Aesar, Heysham, United Kingdom) and used without further purification. Analytical grade sodium hydroxide (NaOH, 97%) and 1,1,1,3,3,3-hexafluoro-2-propanol (F_6-IPA, ≥99%) were purchased (Sigma-Aldrich Inc., St. Louis, USA) and used without further purification. Potassium carbonate (K_2CO_3, >97%) was purchased from Sigma Aldrich, Missouri, USA and used without further purification. Hydrochloric acid (HCl, 36.5-38%) and Nitric acid (HNO_3, 68-70%) were purchased from VWR International, Pennsylvania, USA and used without further purification. Delayed petroleum coke from oil sands bitumen upgrading (Suncor Energy Inc., Alberta, Canada) was ground and sieved to give 150−300 μm diameter particles. Carbon black (Carbon Black Monarch 120, Cabot Corp., Massachusetts, USA) was ground and sieved to give 63−150 μm diameter particles. A commercially available activated carbon, Calgon BPLC, was purchased (Calgon Carbon Corporation, Moon Township, Pennsylvania, USA) ground and sieved to give 150−250 μm diameter particles. Another commercially available activated carbon, Jacobi Ecosorb GX, was purchased (Jacobi Carbons, Kalmar, Sweden), ground and sieved to give 150−250 μm diameter particles.

2.2. Material preparation

The detailed activation and characterization of the petroleum coke and carbon black materials have been reported elsewhere [15,16]. Briefly, these ACs were prepared by chemical activation. The carbon starting material was blended with a chemical agent (KOH, NaOH, or a blend of KOH and K_2CO_3) in a 3:1 mass ratio of the chemical agent to carbon material. The mixture was heated to $T = 1073$ K under a dry N_2 or N_2-steam atmosphere. After heating, the sample was cooled to room temperature before being washed with either aqueous HCl or HNO_3 to neutralize the basic additives. After the material was washed with acid, it was washed with water until p$H = 7$ in the wash water was achieved. The specific details of the preparation for each material are summarized in Table 1.

2.3. Material characterization

The surface area and pore size distributions were determined by N_2 physisorption at $T = 77$ K and CO_2 at $T = 273$ K using a 3Flex (Micromeritics) instrument. Surface area was determined using the methods of Brunaur, Emmett, and Teller [27]. The meso- and macropore sizes were determined by the method of Barrett et al. [28]. For micropore volumes, the t-plot method was used [29]. Finally, the Dubinin-Radushkevich equation [30] was also used to determine the micropore volume from the CO_2 isotherm at $T = 273$ K using the same instrument. Powder X-ray diffraction (XRD) data were obtained using a Rigaku Multiflex diffractometer with a copper target at a speed of 2° min^{-1} and a step size of 0.02°. The powder XRD patterns were obtained using Jade 7.0 software (International Centre for Diffraction Data, ICDD). Scanning electron microscopy (SEM) and energy dispersive X-ray (EDX) analysis were conducted with an FEI quanta 250 FEG SEM equipped with a

Table 1
Activation conditions of the activated carbons.

Sample	Chemical agent	Heat treatment	Acid wash
Petroleum coke material			
P_K [16]	KOH	1073 K, 120 min, N_2 atmosphere	HCl
P_Na [16]	NaOH	1073 K, 120 min, N_2 atmosphere	HCl
P_K/st [16]	KOH	1073 K, 120 min, N_2 and H_2O atmosphere	HCl
P_CK [17]	KOH/K_2CO_3 (0.63:1)	1073 K, 30 min, N_2 atmosphere	HNO_3
Carbon black material			
CB_CK [17]	KOH/K_2CO_3 (0.63:1)	1073 K, 30 min, N_2 atmosphere	HNO_3

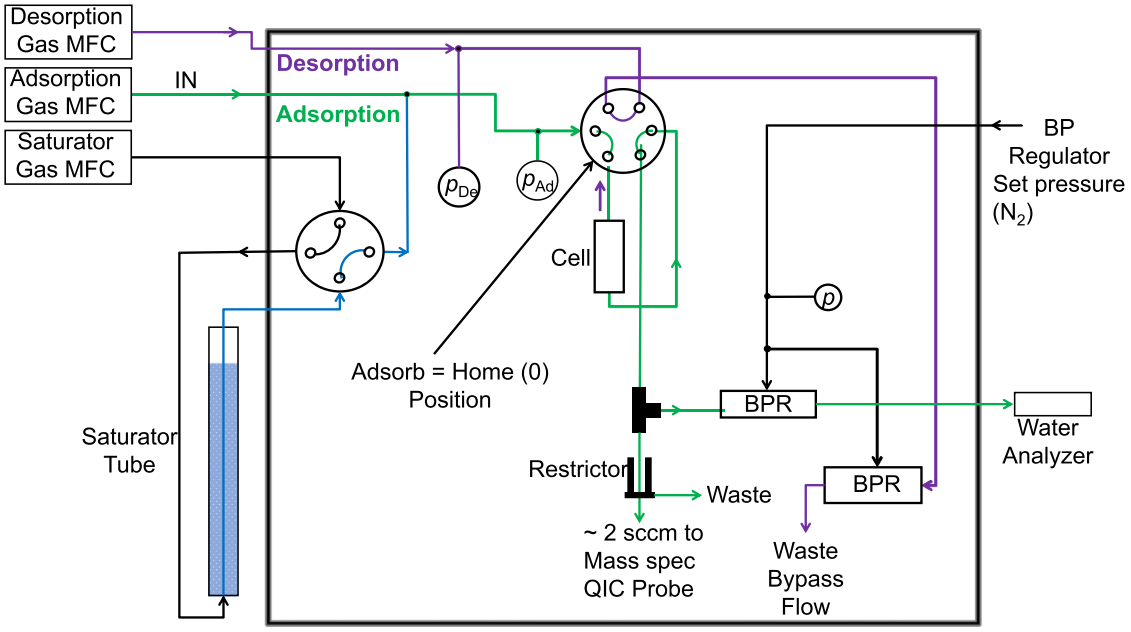

Fig. 1. The schematic of the dynamic adsorption system. Green lines indicate the adsorption plumbing. Purple lines indicate desorption plumbing, and blue lines indicate water-saturated gas. MFC indicates Mass Flow Controller, BP indicates Back Pressure and BPR indicates a Back Pressure Regulator.

GATAN monoCL4 detector and a Brüker Quantax 5030 SDD EDX with Brüker Esprit 2.2 software, respectively.

The surface functionalization of the materials was characterized by XPS (Kratos AXIS Supra, Kratos Analytical (Manchester)) using a monochromatic Al K(α) source (15mA, 15kV). The instrument work function was calibrated to give a binding energy (BE) of 83.96 eV for the Au $4f_{7/2}$ line for metallic gold and the spectrometer dispersion was adjusted to give a BE of 932.62 eV for the Cu $2p_{3/2}$ line of metallic copper. Samples were mounted electrically isolated from the spectrometer and the Kratos charge neutralizer system was used on all specimens. Survey scan analyses were carried out with an analysis area of 300 × 700 microns and a pass energy of 160 eV. High resolution analyses were carried out with an analysis area of 300 × 700 microns and a pass energy of 20 eV. Spectra have been charge-corrected to the main line of the carbon 1s spectrum for graphitic type carbon (C=C) set to 284.5 eV. Shirley backgrounds were used for all spectral processing and spectra were analysed using CasaXPS software (version 2.3.14). Curve-fitting procedures for the C 1s spectra include an asymmetric peak shape for the main peak (graphitic like component) and a pi → pi* shake-up satellite constrained to be 6.41 eV above the main peak with a FWHM of 2.7 eV and an area of 6.93% of the main peak (fittings based on a standard graphite spectrum). All other peaks in the carbon 1s spectra used a 70% Gaussian / 30% Lorentzian (GL(30)) product peak shape, were constrained to have equivalent FWHM and were positioned at binding energies to provide consistent quantification of the various carbon species present. These curve-fitting processes are outlined by Biesinger [31] and are similar to those reported by Morgan [32], Moeini et al. [33] and Gengenbach *et al.* [34]. N 1s spectra were fit with two (GL(30)) peaks of equal FWHM. The peak at 400.0 to 400.2 eV is ascribed to amide and amine type functionality and the second peak at 401.8 to 402.0 eV is ascribed to NR_4^+ type functionality. The O 1s spectra were fit with asymmetric peak shapes for various carbon-oxygen functional groups associated with the graphitic like structures and Gaussian/Lorentzian (GL(30)) shapes for metal oxide(s), silicon oxide and sulfate components. The peak area percentages for metal oxide(s), silicon oxide and sulfate components in the O 1s spectra were constrained to match stoichiometries derived from the survey scan results. Adsorption of F_6-IPA was measured on a TA TGA 550 system. The samples were heated under He flow (25 mL min^{-1}), from T = 296.15 K to T = 723.15 K, to remove any adsorbed species, followed by F_6-IPA adsorption (12% in He) at T = 423.15 K for 3 h.

2.4. Adsorption measurements

2.4.1. Manometric adsorption measurements

Pure gas adsorption isotherms of H_2S, CO_2 and CH_4 were collected on the P_K activated carbon sample at T = 288.15 K and 308.15 K using an in-house built manometric adsorption instrument described elsewhere [7,35–38]. The pure gas adsorption isotherms for H_2S, CO_2, and CH_4 collected at T = 298.15 K were previously reported [7]. Before adsorption, the P_K AC was activated by heating the adsorption cell to T = 423 K under a vacuum of $p = 10^{-10}$ bar.

2.4.2. Gravimetric adsorption measurements

Water adsorption was measured using a continuous-flow thermogravimetric analyzer (SETARAM LABSYSevo TGA) as described in our previous work [37,38]. Water content of the gas stream was controlled

Table 2
Masses of AC materials loaded into the breakthrough columns.

Material	BPLC	P_K	P_K/st	P_Na	P_K/C	CB_K/C	Ecosorb
Mass (g)	0.6149	0.3632	0.2905	0.5199	0.3710	0.4393	0.4531
Packing density ($\times 10^2$ g cm^{-3})	2.356	1.391	1.113	1.992	1.421	1.683	1.736

by three mass-flow controllers with one He stream flowing through a temperature-controlled water saturator, a second He stream connecting to the water saturated He stream and a third He stream flowing through the thermostated balance towards the oven. The water content in the oven can be controlled by adjusting the flow rates of the three He streams. A Honeywell HIH-4010 relative humidity sensor was connected to the TGA outlet to measure the water content of the gas stream. The humidity sensor was externally calibrated by a Meeco MI moisture meter (±0.5% or 0.4 ppmv, whichever was greater). The data handling for these experiments can be found in the supplementary information.

Prior to adsorption measurements, the mass of the TGA support rod and the empty stainless-steel crucible at T = 298 – 423 K and $p_{H_2O} \approx 1 \times 10^{-3} - 3 \times 10^{-3}$ bar was measured. To determine the dry mass of the AC, the stainless-steel crucible was filled with the AC material and heated to T = 423 K while under dry He flow, and the mass of the stainless-steel crucible and the TGA support rod was subtracted.

2.4.3. Dynamic breakthrough measurements

For the multi-component adsorption measurements, an in-house-built dynamic breakthrough instrument was used (Fig. 1). The adsorbent sample was loaded into the test cell (4.6 mm inner diameter × 85 mm length, mass of material in Table 2), which was placed inside a GC oven at the experimental temperature. A heating block was fitted around the test cell for higher temperatures ($T \geq$ 333 K). Adsorption and desorption gases were controlled by mass flow controllers (MFCs, Brooks SLA 5850, 50 Scm^3 min^{-1}), with flow rates verified by an Agilent Technologies ADM 2000 universal flow meter. Water vapor may be added to the adsorb gas feed using a Nafion H_2O saturator tube, which is reported in the literature [39]. A 4-port valve was present for switching the water vapor in and out of the adsorb gas feed, depending on the experiment.

A 6-port diaphragm valve was used to select the flow direction of gases through the cell. Desorb gas and adsorb gas flow in opposite directions through the cell, like commercial adsorption designs. The gas sample flowing out of the cell was detected by a Hiden HPR-20 QIC mass spectrometer (MS, sipping at about 2 Scm^3 min^{-1}), and the data were analyzed using MASoft software. Pressure transducers (Spectre Corporation, model 9000, 0 – 1000 psig) between the MFCs and the 6-port valve allowed recording of the adsorption gas (p_{Ad}) and desorption gas (p_{De}) pressures. Two Equilibar back pressure regulators (BPRs) were introduced to maintain the system's back pressure (via dome loading from a N_2 tank) and ensure a constant flow rate of gas entering the MS probe for analysis. One Equilibar BPR was situated on the feed stream, and the other BPR was located on the bypass stream. The adsorb and desorb gas pressures were balanced using a metering valve. The outlet flow from the Equilibar BPR on the feed stream was also directed to a Meeco moisture meter. Waste gases were directed to a carbon trap and fed to a ventilated bay. Gas pressure recording, valve switching and MASoft data acquisition were controlled with PeakSimple software.

2.5. Data analysis

2.5.1. Manometric adsorption data

All fluid thermodynamic properties were calculated by the appropriate equation-of-state (CO_2 [40], CH_4 [41], H_2S [42], H_2O [43] and He [44]) as provided by Reference Fluid Thermodynamic and Transport Properties V9.1 (REFPROP, NIST) [45]. Mixture densities were calculated following the GERG-2008 [46] mixing rules together with the previously sited reference quality equations-of-state, also implemented within REFPROP.

The methods for determining the amount adsorbed are reported elsewhere for the manometric adsorption experiments [7,35–38]. To determine the moles of adsorptive introduced (n^{int}), the difference in density between the adsorptive in the reference cell before transfer (ρ_{ref}) and the adsorption cell (ρ_{sys}) was multiplied by the volume of the reference cell (V_{ref}).

$$n^{int} = (\rho_{ref} - \rho_{sys}) V_{ref} \tag{1}$$

The amount adsorbed (n^{ads}) was then determined as the sum of the introduced adsorptive minus the amount of adsorptive in the void space of the adsorption chamber,

$$n^{ads} = \sum_{0}^{m} n_m^{int} - \rho_{sys} V_{void} \tag{2}$$

V_{void} is the void volume of the adsorption cell determined by a He expansion of the cell when filled with the adsorbent (He excess adsorption) [47]. An alternative absolute definition of the void volume is to determine the adsorbent volume (V_{mat}) by using the crystal density (ρ_{crys}) and mass of the adsorbent (m_{mat}) and subtracting it from the volume of the adsorption cell (V_{cell}) [48,49].

$$V_{void} = V_{cell} - V_{mat} = V_{cell} - \frac{m_{mat}}{\rho_{crys}} \tag{3}$$

The activated carbon materials are amorphous. As such, the crystal density was determined by taking the inverse of the sum of the bulk carbon crystal volume (V_{bulk}) and the activated carbon pore volume (V_{pore}).

$$\rho_{crys} = \frac{1}{V_{bulk} + V_{pore}} \tag{4}$$

The method of determining the uncertainty for the manometric adsorption system has been previously reported [35–38]. Briefly, the 95% confidence interval uncertainty was calculated for n^{ads} at each measured pressure. The uncertainty for the amount adsorbed can be calculated by the propagation of random error from the uncertainty in density, pressure, temperature, reference volume, material mass, and void volume. The uncertainties for the manometric experimental data have been reported in Tables S4–S6 of the SI.

2.5.2. Gravimetric adsorption data

For this work, the method of Murata *et al.* was used to determine the displacement of the gas phase by the adsorbent–adsorbate volume with the assumption that the adsorbent–adsorbate volume was fixed by the crystal density and mass of the adsorbent [50].

$$n^{ads} = n^{ob} + \rho_{bulk} \cdot \left(\frac{M_{mat}}{\rho_{mat}}\right) - \left(\frac{B}{M_{mat}}\right) \tag{5}$$

where n^{ads} is the absolute amount adsorbed, n^{ob} is the measured mass, ρ_{bulk} is the bulk phase density, M_{mat} is the mass of the material, ρ_{mat} is the density of the material, and B is the dry mass. This definition defines all adsorption as absolute (not excess adsorption). The crystal density was determined as described in Eq. (4).

2.5.3. Dynamic breakthrough data

The start time (t =0) for each breakthrough run was determined by the breakthrough time of a He tracer in the gas mixture. The breakthrough time of all species was determined by fitting a linear equation to the range of c/c_0 = 0.1 – 0.5 (where c/c_0 is the concentration measured

at the outlet of the breakthrough column divided by the initial concentration of the gas mixture) and taking the *x*-intercept of the equation to be the breakthrough time, *i.e.*, onset time. The equilibrium amount adsorbed (n^{ads}) of each species on the materials was determined from the difference of moles introduced (moles in, n^{in}) and moles exciting the column (moles out, n^{out}) divided by the mass of the adsorbent (m_{mat}).

$$n_i^{ads} = \frac{n_i^{in} - n_i^{out}}{m_{mat}} \tag{6}$$

The n^{in} was determined by integrating the molar flow rate (F_i) of species *i* over the time of the breakthrough experiment.

$$n_i^{in} = \int_0^{t^\infty} F_i \, dt \tag{7}$$

Similarly, the n^{out} was determined by integrating the product of F_i and c/c_0 of species *i* over the time of the breakthrough experiment.

$$m_i^{in} = \int_0^{t^\infty} F_i \frac{c_i}{c_{0,i}} dt \tag{8}$$

As stated earlier, the uncertainties for the adsorbed equilibrium amounts can be calculated at the 95% confidence interval by the random error propagation. Alternatively, two times the standard deviation of triplicate measurements can be used as the uncertainty for the amounts adsorbed. The uncertainties reported are of the greatest value between the two methods.

2.6. Modelling

2.6.1. Isotherm modelling

The Langmuir isotherm equation was fit to the pure component adsorption data for this work [51].

$$n^{ads} = n^\infty \frac{bf}{1+bf} \tag{9}$$

where n^∞ is the adsorption capacity, *b* is the adsorption affinity constant, and *f* is the fugacity of the adsorptive. The Langmuir equation can be expanded to account for temperature dependence.

$$b = b^\circ \exp\left(-\frac{\Delta H}{RT}\right) \tag{10}$$

Here b° corresponds to the infinite adsorption constant, ΔH corresponds to the isosteric heat of adsorption and *R* is the gas constant. The fit for the Langmuir equation of each species was optimized by minimizing the mean sum of square errors (MSSE) across the different temperatures.

In this work, the isosteric heat of adsorption of the pure components was calculated *via* the equations derived by Hückel [52]. The isosteric heat is estimated by calculating the fugacity (*f*) corresponding to the amount adsorbed at different temperatures [53].

$$\Delta H = -RT \left(\frac{\partial ln f}{\partial T}\right)_{n^{ads}} \tag{11}$$

Using a cubic spline fit to interpolate the experimental data (for constant n^{ads}), the fugacity at any amount adsorbed can be determined without prior fitting to an isotherm equation [35–38]. The isosteric heat of adsorption was only calculated in ranges where the amount adsorbed had been experimentally determined. Alternatively, the fugacity at defined amounts adsorbed can be calculated using the Langmuir isotherm fits for the pure component data.

2.6.2. Multicomponent modelling

Four different multi-component adsorption models are compared to the experimental results in this work. The first model is the dual-site competitive Langmuir isotherm equation [25].

$$n_1^{ads} = n_1^\infty \frac{b_1 p f_1}{1 + b_1 f_1 + b_2 f_2 + b_3 f_3} \tag{12}$$

$$n_2^{ads} = n_1^\infty \frac{b_2 f_2}{1 + b_1 f_1 + b_2 f_2 + b_3 f_3} + \frac{\left(n_2^\infty - n_1^\infty\right) b_2 f_2}{1 + b_2 f_2 + b_3 f_3} \tag{13}$$

$$n_3^{ads} = n_1^\infty \frac{b_3 f_3}{1 + b_1 f_1 + b_2 f_2 + b_3 f_3} + \frac{\left(n_2^\infty - n_1^\infty\right) b_3 f_3}{1 + b_2 f_2 + b_3 f_3} \tag{14}$$

where n_i^{ads} is the amount adsorbed of species *i*, n_i^∞ and b_i are the adsorption capacity and adsorption affinity constant obtained from the pure component Langmuir isotherm equation for species *i*.

The second model used is the ideal adsorbed solution theory (IAST) derived by Myers and Prausnitz [26].

$$f_i = x_i f_i^\circ(\pi) \tag{15}$$

where x_i is the adsorbate mole fraction and $f_i^\circ(\pi)$ is a hypothetical pure component adsorbate fugacity that gives an equivalent spreading pressure (π) for all components. To simplify the calculations, the reduced spreading pressure (z) is introduced.

$$z = \frac{\pi A}{RT} = \sum_{i=1}^{N} y_i \int_0^{f_i} \frac{n_i^{ads}}{f_i} df_i \tag{16}$$

where y_i is the adsorptive mole fraction, this work used the analytical solutions for the spreading pressure derived from the Langmuir isotherm equation.

$$z = n_i^\infty \ln\left(1 + b_i f_i^\circ\right) \tag{17}$$

The third model used is a multi-component model developed by Wynnyk for high-pressure adsorption systems [35]. The model uses an iterative approach to solve for adsorption equilibrium. The amount adsorbed of each species ($n_{i,q}^{sc}$) is calculated as a function of fugacity and the infinitesimal mass (*q* or *m/F*), where there are a total of *F* infinitesimal elements,

$$n_{i,q}^{sc} = \left(Isotherm\left[f_{i,q}^{EOS}\left(p, T, y_{i,q}\right), T\right]\right) \cdot \frac{m}{F} \tag{18}$$

and the moles in the adsorptive phase ($n_{bulk,i,q}$) divided by the sum of moles in the adsorptive phase for all species gives $y_{i,q}$ and $n_{bulk,i,q}$ is the difference of the initial assumption and the last calculated value of $n_{i,q}^{mc}$.

$$y_{i,q} = \frac{n_{bulk,i,q}}{\sum_i^j \left(n_{bulk,i,q}\right)} \tag{19}$$

$$n_{bulk,i,q} = n_{bulk,i,initial} - \sum_1^F n_{i,q}^{mc} \tag{20}$$

The final method to predict the multi-component system used the partial pressures of the individual components of the mixtures to determine the amounts adsorbed with no further account of the interactions between species.

The models presented in this work were used to calculate the selectivity between species *i* and *j* (S_{ij}). The selectivity can be defined as the ratio of the partition coefficients (*K*) of *i* and *j*. The partition coefficient describes the amount adsorbed of species i divided by the mole fraction of species *i*.

$$S_{ij} = \frac{K_i}{K_j} = \frac{n_i / y_i}{n_j / y_j} \tag{21}$$

The models were compared to the experimental results using % residual.

$$\%\ \text{residual} = \frac{(model - experimental)}{experimental} \times 100\% \tag{22}$$

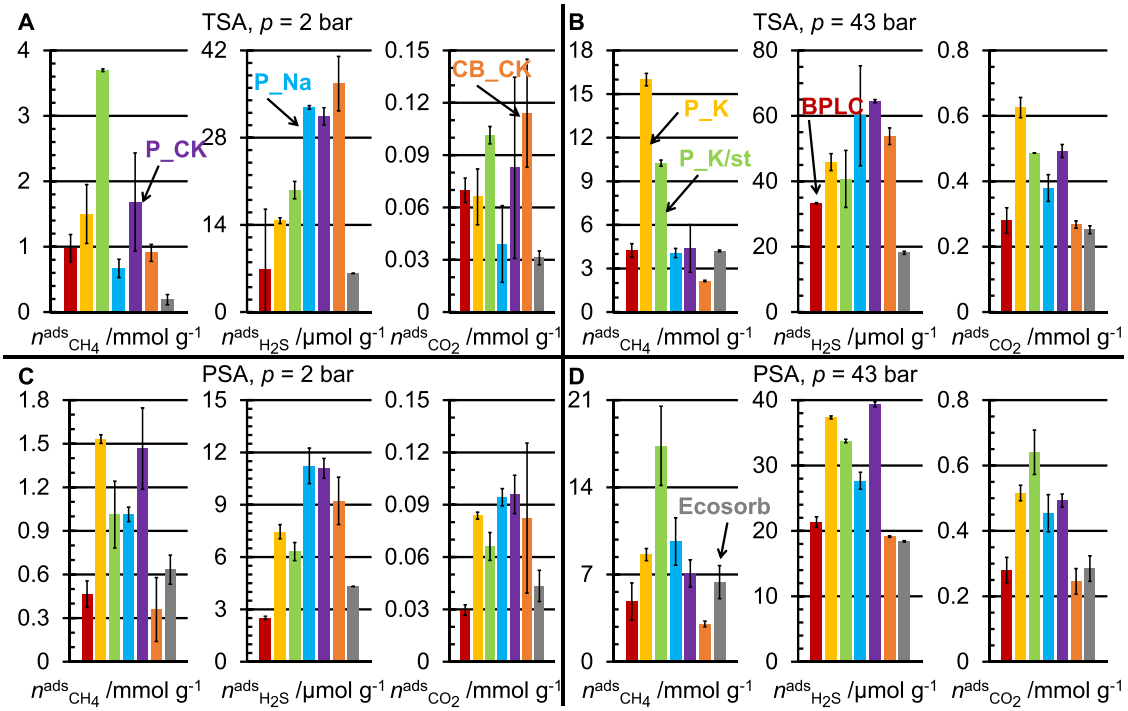

Fig. 2. The amounts adsorbed for the TSA (A, B) and PSA (C, D) experiments at low pressure (p = 2 bar, T = 302.7 ± 0.5 K, A, C) and high-pressure (p = 43 bar, T = 302.7 ± 0.5 K, B, D) for the ACs (BPLC, red, p = 1.94 ± 0.04 bar, p = 43.0 ± 0.2 bar; P_K, p = 2.14 ± 0.05 bar, p = 43.06 ± 0.06 bar, yellow; P_K/st, p = 2.14 ± 0.05 bar, p = 42.93 ± 0.04 bar, green; P_Na, p = 2.13 ± 0.05 bar, p = 42.9 ± 0.2 bar, blue; P_CK, p = 2.13 ± 0.05 bar, p = 42.9 ± 0.1 bar, purple; CB_CK, p = 2.20 ± 0.02 bar, p = 42.95 ± 0.03 bar, orange; Ecosorb, p = 1.93 ± 0.05 bar, p = 42.9 ± 0.2 bar, grey) are presented.

2.7. Gibbs energy minimization

To calculate the equilibrium concentrations of the COS formation reaction, a Gibbs energy minimization (GEM) routine was completed as described in the literature [54–56]. The first step of the GEM routine is the calculation of the standard state Gibbs energy of formation ($\Delta_f G_i^o$) for species i using the enthalpy and entropy values reported in the Joint Army, Navy, Air Force (JANAF) thermochemical tables [57]. Using the fugacities calculated by REFPROP and the standard state Gibbs Energy of formation for each species, Eq. (20) can be solved iteratively by minimizing the total Gibbs Energy function using both the Solver tool and the Generalized Reduced Gradient within Microsoft Excel.

$$G(T,p) = \sum_{i=1}^{N} y_i \left[\Delta_f G_i^o + RT ln\left(y_i \phi_i p\right)\right] \tag{23}$$

where ϕ_i is the fugacity coefficient of species i. We note that the enthalpy of formation for COS has been corrected according to Deering et al. [54].

2.8. Multiple component regression analysis

To assess the significance of the material properties to the experimental capacities and selectivities, a multiple component regression analysis was conducted using the Regression data analysis tool built into Microsoft Excel:

$$y = b_0 + \sum_{i}^{N} b_i x_i \tag{24}$$

where b_0 is the intercept and b_i is the slope corresponding to the variable x_i. A stepwise elimination of the variables was conducted where the variable with the lowest magnitude t stat was eliminated until the minimum standard error was achieved. For this analysis, if the standard error was greater than 20% of the average y value, then there was no significant trend for that y parameter.

3. Results and discussion

3.1. Material characterization

Characterization of the carbon samples by N_2 and CO_2 physisorption is presented in Table 3. These results show that the P_K, P_K/st and P_CK materials have the highest BET apparent surface areas among the samples tested. All samples except for P_K/st and Ecosorb had a similar percentage of the total surface area (56-68%) from micropores. Interestingly, materials P_K/st, CB_CK and Ecosorb were the only materials with 50% or more of the pore volume from macropores (> 50 nm diameter). The results from the surface area characterization and porosity agree with the previous publications of the P_K, P_K/st, P_Na, P_CK and CB_CK materials [15–17].

Elemental analysis by XPS revealed that all materials were greater than 90% carbon (91-96%) (Table 4), with oxygen (3.9-7.3%) being the only other significant element present in the materials. It is interesting to note that BPLC, P_Na, P_CK, and Ecosorb materials showed traces of iron (Fe) in the analysis (0.1–0.2 %) and P_K, P_K/st and P_CK showed traces of nitrogen (N; 0.2-0.4%). Further investigation into the functional group distribution of the carbon and oxygen peaks is presented in Table 4. When the peaks for carbon and oxygen are deconvoluted, the analysis shows that the BPLC and Ecosorb ACs had the highest mineral content, accounting for most of the oxygen found in the elemental analysis. For the petcoke ACs, the P_K/st AC had the lowest functional group concentration on the surface, while the other three petcoke ACs had similar functional group concentrations. Comparing the XPS and EDX techniques showed good agreement between the elemental analyses, further validating these presented XPS results. It is important to note that the uncertainty in the EDX measurements was greater than in the XPS measurements for the results reported. For example, the average uncertainty on the percent carbon from the EDX experiments was 22%, while the XPS measurements reported a maximum uncertainty of 0.5% for all elements.

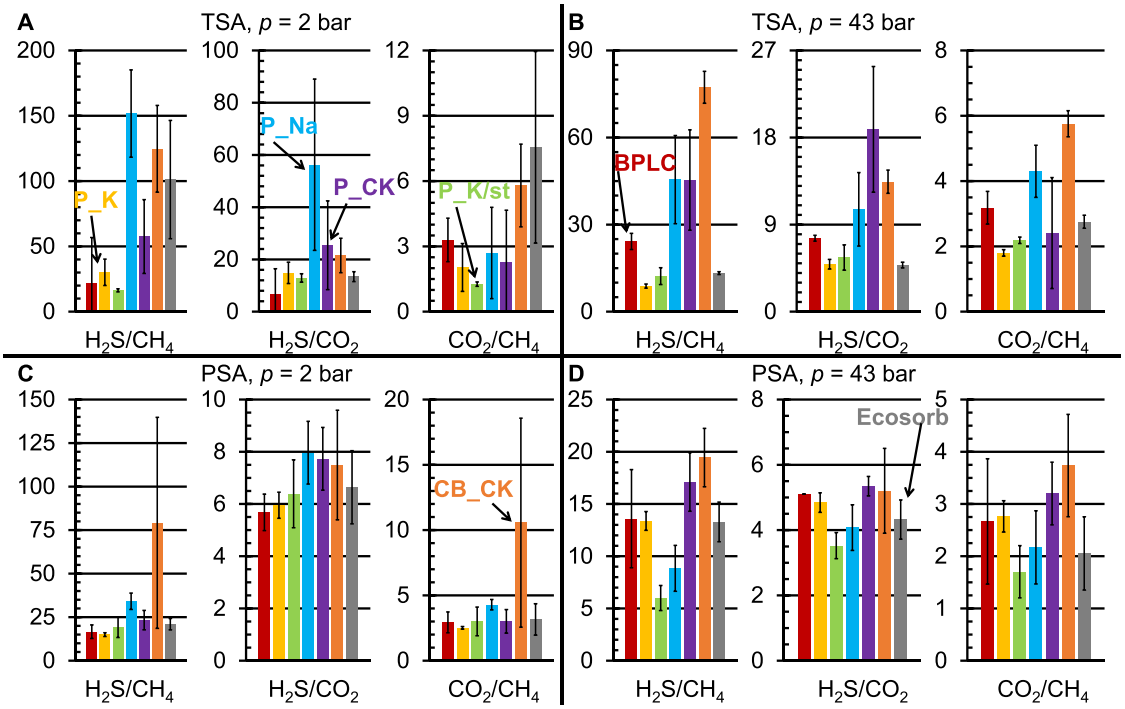

Fig. 3. The selectivities for the TSA (A, B) and PSA (C, D) experiments at low pressure (p = 2 bar, T = 302.7 ± 0.5 K, A, C) and high-pressure (p = 43 bar, T = 302.7 ± 0.5 K, B, D) for the ACs (BPLC, red, p = 1.94 ± 0.04 bar, p = 43.0 ± 0.2 bar; P_K, p = 2.14 ± 0.05 bar, p = 43.06 ± 0.06 bar, yellow; P_K/st, p = 2.14 ± 0.05 bar, p = 42.93 ± 0.04 bar, green; P_Na, p = 2.13 ± 0.05 bar, p = 42.9 ± 0.2 bar, blue; P_CK, p = 2.13 ± 0.05 bar, p = 42.9 ± 0.1 bar, purple; CB_CK, p = 2.20 ± 0.02 bar, p = 42.95 ± 0.03 bar, orange; Ecosorb, p = 1.93 ± 0.05 bar, p = 42.9 ± 0.2 bar, grey) are presented.

Table 3
N_2 physisorption results and F_6-IPA adsorption results on the ACs.

	BPLC	P_K	P_K/st	P_Na	P_CK	CB_CK	Ecosorb
A_{BET} /m^2 g^{-1}	1109	2684	3051	1097	2762	474	1307
$A_{micropore}$ /%	59	56	9	63	68	59	27
V_{p,N_2} /cm^3 g^{-1}	0.57	1.35	1.90	0.73	1.34	0.57	0.78
V_{p,CO_2} /cm^3 g^{-1}	0.52	0.66	0.58	0.59	0.68	0.48	0.49
$V_{p,micropore}$ /cm^3 g^{-1}	0.30	0.69	0.13	0.31	0.83	0.13	0.18
$V_{micropore}$ /%	52	51	7	43	62	22	23
$V_{mesopore}$ /%	16	11	23	26	9	28	17
$V_{macropore}$ /%	32	38	70	31	29	50	60
$n^{ads}_{F6\text{-}IPA}$ /µmol g^{-1}	1.1	1.1	0.76	0.13	1.2	0.18	0.99
$n^{ads}_{F6\text{-}IPA}$ /wt%	19	18	13	2.2	19	3.1	17

Table 4
Material elemental composition (atomic %) and C deconvolution results from XPS and EDX analysis.

	BPLC XPS [EDX]	P_K XPS [EDX]	P_K/st XPS [EDX]	P_Na XPS [EDX]	P_CK XPS [EDX]	CB_CK XPS [EDX]	Ecosorb XPS [EDX]
B	-	0.3	0.3	-	-	-	-
C	93.1 [87.6]	91.4 [93.1]	93.6 [92.1]	93.7 [94.7]	92.6 [92.2]	95.9 [91.1]	92.2 [91.1]
N	-	0.2	0.4	-	0.2	-	-
O	5.5 [9.4]	7.3 [6.8]	5.0 [7.7]	5.7 [5.0]	6.5 [7.8]	3.9 [8.7]	5.4 [6.4]
Na	-	-	-	0.1	-	-	-
Al	0.5 [1.4]	0.1	0.1	0.1	0.1	-	0.8 [1.1]
Si	0.7 [3.9]	0.2	0.1	0.2	0.2	0.1	1.0 [1.5]
P	- [0.2]	-	0.1	-	-	-	-
S	0.1 [0.2]	0.1	0.4 [0.2]	-	0.2	0.1 [0.2]	0.1 [0.3]
Ca	- [0.8]	-	-	-	-	-	0.3 [0.8]
Fe	0.1 [0.2]	-	-	0.2	0.2	-	0.1 [0.3]
Functional groups (C)							
O-C=O	2.7	4.6	3.7	4.2	4.3	2.3	2.1
C=O	3.0	4.7	3.5	4.5	4.4	2.8	2.3
C-OH, C-O-C	5.5	8.7	6.0	7.6	8.2	4.4	5.7
C=C	88.8	82.1	86.9	83.8	83.2	90.5	89.9

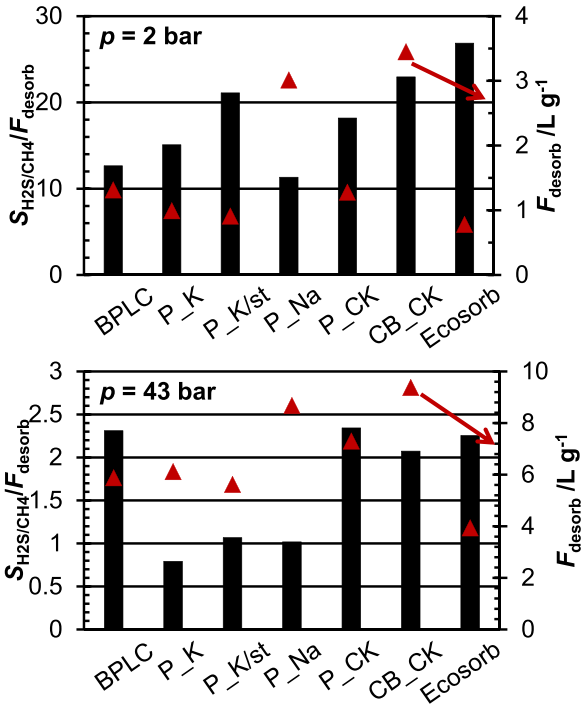

Fig. 4. A comparison of PSA selectivities and desorption volumes for the different ACs at low-pressure (top) and high-pressure (bottom) measurements. The bar graph represents the ratio of selectivity, and the desorption volume for each AC and the red triangles represent the desorption volume of the ACs.

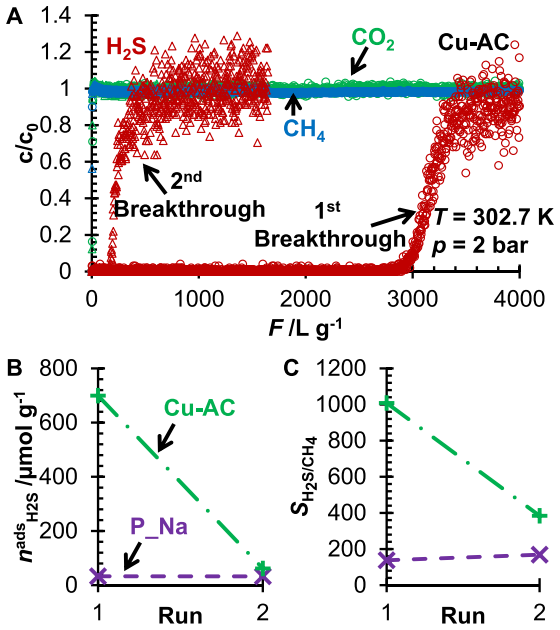

Fig. 5. The breakthrough experiments for the Cu impregnated AC (A), H_2S (red), CH_4 (blue) and CO_2 (green) with ○ symbols for the first breakthrough and Δ for the replicated experiment. The amount of H_2S adsorbed (B), and the H_2S/CH_4 selectivity (C) of the P_Na AC (purple, ×, ▬) and Cu impregnated AC (green, +, ▬ •) for the first breakthrough run and the replicate experiment.

The surface basicity is believed to play an important role in the selectivity of acid gases; hence, another characterization performed on the ACs was a surface basicity estimation from the adsorption of the weak acid, F_6-IPA, at T = 423.15 K. This methodology has previously been used to analyze the relative acidity of zeolites and similar materials for catalysis applications [58]. This technique was chosen over techniques such as the Boehm titration as the mass of the petcoke sample materials was limited. The results of the F_6-IPA adsorption are presented in Table 3. These results show that the P_CK and BPLC ACs adsorbed the most F_6-IPA, while P_Na and CB_CK adsorbed the least. This indicates that, P_CK and BPLC have the most basic surfaces, while P_Na and CB_CK have the least basic surfaces.

3.2. Multi-component adsorption results

The performance of the materials in both temperature swing (TSA) and pressure swing adsorption (PSA) applications were examined. For the TSA experiments, the adsorbents were activated by flowing N_2 at the pressure of the experiment while the AC bed was heated to T = 723 K for 12 h. Note that each experiment was reproduced in triplicate. For the PSA experiments, the AC bed was activated by flowing N_2 at the experimental pressure without an increase in temperature until the CH_4, H_2S or CO_2 concentrations on the MS were stable. To ensure no bed effects, the P_K and BPLC samples were run at p = 2 bar and T = 302.7 ± 0.5 K using two different bed sizes (P_K bed size = 98 or 363 mg, BPLC bed size = 155 or 615 mg). The multi-component adsorption experiments showed no difference between the small and large bed experiments.

The results of the breakthrough experiments are shown in Figs. 2 and 3. The amounts adsorbed for CH_4, H_2S and CO_2 on the ACs at T = 302.7 ± 0.5 and p = 2 and 43 bar for both TSA and PSA experiments are presented in Fig. 2. P_Na, P_CK and CB_CK had the highest H_2S adsorption capacity in all experiments except for the high-pressure PSA experiment, where P_CK, P_K and P_K/st had a higher capacity than P_Na and CB_CK. The selectivities for H_2S/CH_4, H_2S/CO_2 and CO_2/CH_4 of the ACs were calculated from the experimental data and are presented in Fig. 3. For the low-pressure TSA experiments, the P_Na AC had the highest selectivity for H_2S/CH_4 (S_{H_2S/CH_4} = 152) and H_2S/CO_2 (S_{H_2S/CO_2} = 56), with Ecosorb having the highest selectivity for CO_2/CH_4 (S_{CO_2/CH_4} = 7.6). This observation was in contrast to the results found for the low-pressure PSA experiments, where CB_CK had the highest H_2S/CH_4 (S_{H_2S/CH_4} = 79) and CO_2/CH_4 (S_{CO_2/CH_4} = 11) selectivity, while P_Na still had the highest selectivity for H_2S/CO_2 (S_{H_2S/CO_2} = 8.0). In the high-pressure TSA experiments, CB_CK again had the highest H_2S/CH_4 (S_{H_2S/CH_4} = 77) selectivity and the highest CO_2/CH_4 (S_{CO_2/CH_4} = 5.8) selectivity. P_CK had the highest H_2S/CO_2 (S_{H_2S/CO_2} = 19) selectivity under these conditions. In the high-pressure PSA experiments, CB_CK had the highest H_2S/CH_4 (S_{H_2S/CH_4} = 19) and CO_2/CH_4 (S_{CO_2/CH_4} = 3.7) selectivities, and P_CK had the highest H_2S/CO_2 (S_{H_2S/CO_2} = 5.3) selectivity. With Fig. 3, the selectivity for H_2S/CH_4 consistently decreased under a higher pressure for all samples. The selectivity of H_2S/CO_2 was also reduced for all samples except for BPLC, where the selectivity increased with pressure for the TSA experiments.

From the TSA experiments, it should be noted that of the petcoke ACs investigated, P_Na and P_CK show the greatest potential as TSA adsorbents, while CB_CK is also a strong candidate. CB_CK shows the greatest promise for the PSA experiments based solely on selectivity. The desorption of H_2S in the PSA experiments was compared with the H_2S/CH_4 selectivity by taking the ratio of selectivity and desorption volume (S_{ij}/F_{desorb}) (Fig. 4). Comparing the ratio of selectivity to the regeneration volume provides an estimate for the performance *vs.* similar pressure drop, thus a material with a larger S_{ij}/F_{desorb} would require less pressure drop for a similar separation performance. From the analysis of the PSA selectivities and desorption volumes, Ecosorb had the best selectivity ratio to desorption volume and the P_K/st, and CB_CK ACs would be the following best materials for the PSA process at low pressures. The P_CK AC had the highest selectivity ratio for the high-pressure experiments, while the BPLC and Ecosorb ACs showed the next highest ratios. The Ecosorb AC showed the lowest desorption volumes

Table 5
Amounts adsorbed and selectivities for multi-component H_2S mixtures from the literature and experiments of this work.

Material	T /K	p /bar	Composition	H_2S n^{ads}/mmol g^{-1}	CO_2 n^{ads}/mmol g^{-1}	CH_4 n^{ads}/mmol g^{-1}	S_{H_2S/CH_4}	S_{H_2S/CO_2}
Zeolite 4A	308.15	6.25	47:53	-	-	-	-	2.0
[59]		5.91	58:42	-	-	-	-	1.8
		6.18	65:35 CO_2/H_2S	-	-	-	-	1.9
Zeolite 4A	298.15	68.1	0.7499:0.1305:0.1196	1.95	2.13	0.95	12.87	1.00
[35]			$CH_4/CO_2/H_2S$					
Zeolite 5A	308.15	6.25	63:37	-	-	-	-	5.4
[59]			CO_2/H_2S					
Zeolite 13X	308.15	6.32	66:34	-	-	-	-	11.9
[59]			CO_2/H_2S					
Zeolite 13X	298.15	4.04	0.7499:0.1305:0.1196	0.37	0.40	1.31	1.77	1.01
[35]		45.7	$CH_4/CO_2/H_2S$	2.22	2.36	1.65	8.44	1.03
		83.5		2.49	2.02	1.57	9.94	1.35
MIL-101(Cr)	298	1.01	1:10:89	0.4	0.8	-	-	5
[60]			$H_2S/CO_2/He$					
Ce-BTC [60]	298	1.01	1:10:89	0.109	0.126	-	-	11.6
			$H_2S/CO_2/He$					
ZIF-8 [60]	298	1.01	1:10:89	0.07	0.05	-	-	7.2
			$H_2S/CO_2/He$					
P_Na (This	302.7	2.13	0.9396:0.0204:0.0003:0.0397	0.011	0.094	1.01	34	8
work)		42.9	$CH_4/CO_2/H_2S/He$	0.028	0.45	9.6	9	4.1
P_CK (This	302.7	2.13	0.9396:0.0204:0.0003:0.0397	0.0111	0.010	1.5	23	8
work)		42.9	$CH_4/CO_2/H_2S/He$	0.0394	0.49	7.1	17	5.3
CB_CK (This	302.7	2.20	0.9396:0.0204:0.0003:0.0397	0.009	0.08	0.4	79	7
work)		42.95	$CH_4/CO_2/H_2S/He$	0.019	0.25	3.0	19	5

for both low- and high-pressure PSA experiments. For the petcoke ACs, the P_K/st AC had the lowest desorption volumes, and the P_Na AC had the highest. It is important to acknowledge that while the CB_CK and P_Na ACs had some of the highest selectivities, they also had some of the highest uncertainties in the selectivity.

Table 5 was compiled from reviewing the literature for adsorption of multi-component gas mixtures, including H_2S on zeolites and MOFs. This table only includes experimental results for the amount adsorbed and selectivity of physisorption systems. In the case of MOFs, it only presents the three materials with the highest selectivity for physisorption. This research is focused on physisorption separations as milder regeneration conditions are required to regenerate the materials.

In Table 5, the results from the PSA experiments were chosen over the TSA as it would best reflect the separation based solely on physisorption. Comparing the H_2S/CH_4 selectivities of the ACs to zeolites 4A and 13X, it is apparent that both P_CK and CB_CK showed much higher selectivities at higher pressures than either 4A or 13X. The H_2S/CO_2 selectivities comparison showed that the ACs generally exhibited a higher selectivity than the zeolites. Still, it is difficult to make a clear comparison with varying temperatures, pressures, and compositions. When the AC selectivities are compared to the MOFs', it is noted that only the Ce-BTC MOF has a higher H_2S/CO_2 selectivity than the ACs presented in Table 5. Overall, the ACs are competitive with the zeolites and MOFs for H_2S and CO_2 separations. Furthermore, another important consideration is that the ACs studied in this work are unmodified with functional groups or species known to react with H_2S for increased selectivity (*e.g.,* amines, copper, iron, KOH, *etc*.).

Chemisorption materials were not investigated or compared because they are often single-use materials. For example, the sour gas breakthrough at T = 307.5 K and p = 2 bar was collected on a copper (Cu) impregnated AC (Cu-AC) (Fig. 5). Initially, the Cu-AC showed a very high H_2S/CH_4 selectivity (S_{H_2S/CH_4} = 1008). After regenerating under the same conditions as the other ACs, the selectivity dropped to less than half the initial selectivity. While the selectivity of the second run was still high (S_{H_2S/CH_4} = 384), the material would likely last for 3-4 breakthroughs before the capacity is subject solely to the interactions of the AC and not the impregnated material. The duplicate results for the P_Na AC are presented in Fig. 5, and the P_Na has a stable amount of H_2S adsorbed while the amount adsorbed on Cu-AC decreased significantly ($\Delta n^{ads}_{H_2S}$ = 91%, $\Delta S_{H_2S/CH_4}$ = 62%) after a single replicate. These results are not surprising, as Boudou et al. [61] measured H_2S adsorption on amine-modified ACs and demonstrated that the H_2S capacity dropped by 20% over four adsorption cycles. Hamon *et al.* showed that MIL-101(Cr) and MIL-101(Fe) displayed irreversible H_2S adsorption [62]. Materials with dominant physisorption mechanisms are better suited for long-term use than chemisorption materials.

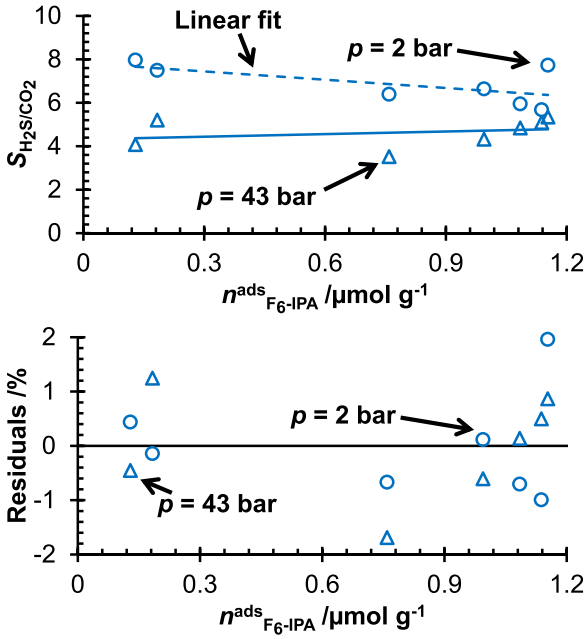

Fig. 6. The H_2S/CO_2 selectivity (p = 2 bar, ○, ▬ ▬; p = 43 bar, Δ, ▬) against the amount of F_6-IPA adsorbed on the ACs (top). The residuals to the linear fit (bottom).

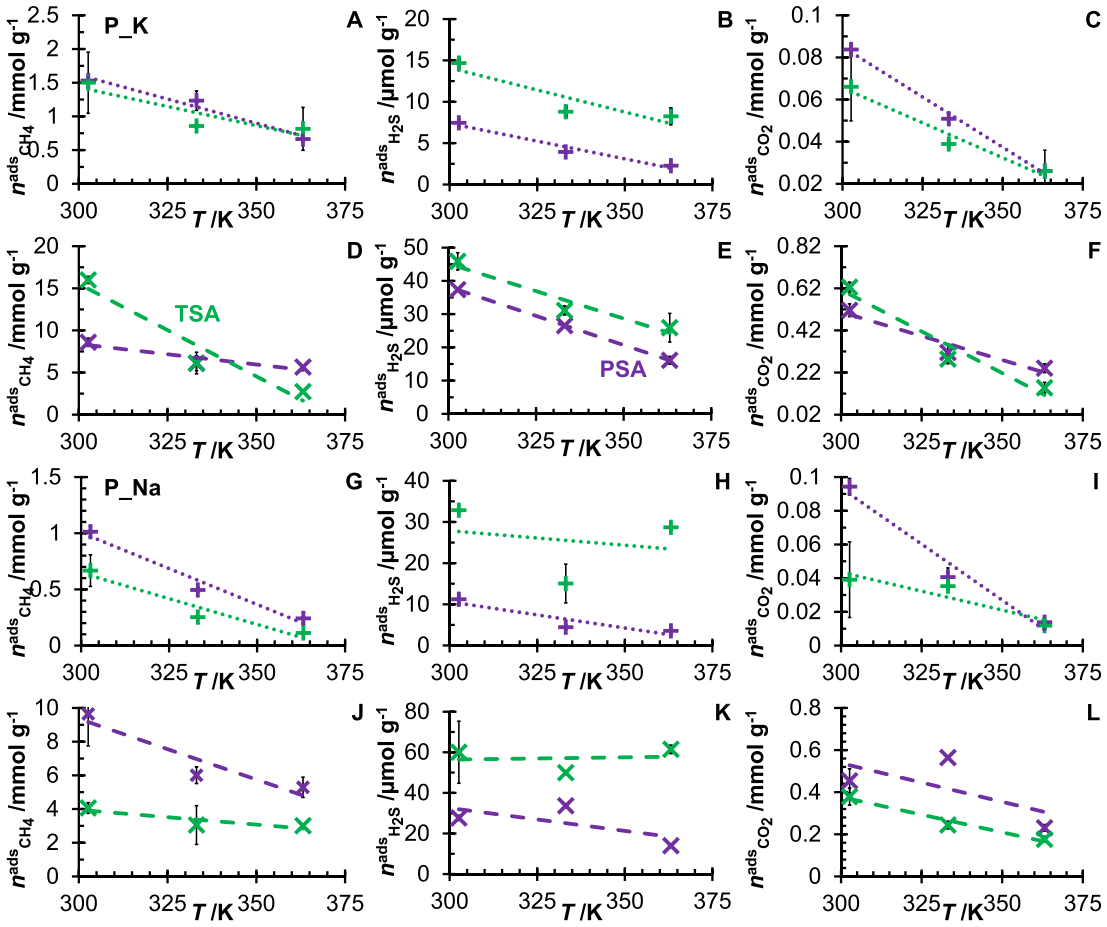

Fig. 7. The amounts adsorbed of CH_4 (A, D, G, J), H_2S (B, E, H, K) and CO_2 (C, F, I, L) on P_K (A–F) and P_Na (G–L) at various temperatures. For all plots, the results for TSA (green) and PSA (purple) experiments at p = 2 bar (+, • •) and p = 43 bar (×, ▬ ▬) are reported. Lines represent linear fits.

Table 6
The results of the multiple component regression analysis.

		p /bar	b_i S_{BET} /10^3 m^2 g^{-1}	%C	%O	%O-C=O	%C=O	%C-OH	Standard error /%
K_{CH_4}	TSA	2	1.0 ± 0.1	-	0.15 ± 0.08	2.8 ± 0.3	-	-29 ± 2	11
	PSA	2	0.155 ± 0.004	0.181 ± 0.009	-	-0.73 ± 0.02	-4.9 ± 0.3	15.1 ± 0.5	0.6
K_{H_2S}	TSA	2	-	63 ± 13	-125 ± 41	-	2791 ± 813	-	20
	TSA	43	-	22 ± 7	-	-	529 ± 100	-	15
	PSA	2	-	16 ± 4	-42 ± 12	-	917 ± 228	-	16
	PSA	43	-	13 ± 3	86 ± 9	-76 ± 11	-2887 ± 256	2215 ± 208	3
K_{CO_2}	TSA	2	1.20 ± 0.04	-	1.44 ± 0.04	0.9 ± 0.1	-	-38 ± 1	2
	TSA	43	4.0 ± 0.9	-	-	-	37 ± 9	-	10
	PSA	2		2.02 ± 0.08	-3.2 ± 0.2	-1.9 ± 0.3	57 ± 6	37 ± 5	2
	PSA	43	-	7 ± 1	-	-	-258 ± 52	323 ± 55	12
S_{H_2S/CH_4}	PSA	2	-	23 ± 3	-64 ± 8	-	1774 ± 187	-505 ± 65	9
	PSA	43	-	-	5.0 ± 0.9	-9 ± 2	-	-	16
S_{H_2S/CO_2}	PSA	2	-	1.7 ± 0.6	-5 ± 2	-	94 ± 38	-	9
	PSA	43	-	-0.7 ± 0.4	2 ± 1	-1.5 ± 0.5	-28 ± 23	-	8
S_{CO_2/CH_4}	TSA	2	0.34 ± 0.04	1.60 ± 0.06	-6.6 ± 0.2	-5.23 ± 0.09	156 ± 4	-	1
	TSA	43	-	-	-6 ± 2	5 ± 2	200 ± 46	137 ± 28	14
	PSA	2	-	3.1 ± 0.7	-5 ± 2	-3.3 ± 0.9	130 ± 45	-	17
	PSA	43	-	-	1.8 ± 0.5	-2.5 ± 0.5	-31 ± 14	21 ± 9	5

3.2.1. *Adsorption correlation investigation*

An investigation into the trends regarding the physical properties of the material (surface area and porosity) and the amount adsorbed was conducted. Table 6 summarizes the slopes and the standard error from the multiple regression analysis between the partition coefficients and selectivities to the material properties. This table only shows the results deemed significant (95% confidence error ≤ 20% of the average y). The adsorption of CH_4 correlated with the BET apparent surface area, carboxylate group fraction, carbonyl groups fraction, and hydroxyl group fractions (from XPS analysis) of the ACs, with the hydroxyl group fraction showing the largest magnitude slope/correlation. It should be noted that only the regression analysis with low-pressure data had a expanded error below the significance chosen. For H_2S, the adsorption properties are best correlated with the carbon percent and carbonyl

groups fraction determined from XPS analysis. For both the PSA and TSA experiments, at all tested pressure, a positive correlation was observed for the carbon percent, while the carbonyl groups had a positive correlation for all experiments except for the high-pressure PSA experiment, where a negative trend was observed. The carbonyl groups fraction had the largest slope of the fitted parameters. Lastly, the adsorption of CO_2 best correlated with the BET apparent surface area for the TSA experiments, while the PSA experiments correlated best with the carbonyl group fraction and hydroxyl/ether groups fraction determined from XPS analysis. The results for H_2S and CO_2 are in agreement with the literature, which shows that increasing the concentration of oxygen-containing functional groups increases the amount of H_2S and CO_2 adsorbed [63,64]. Only the PSA experiments showed significant correlations from the multiple regression analysis of the H_2S/CH_4 and H_2S/CO_2 selectivities. The H_2S/CH_4 selectivity for the low-pressure experiments correlated to the carbon percent (positive), oxygen percent (negative), carbonyl group fraction (positive) and hydroxyl group fraction (negative). The high-pressure H_2S/CH_4 selectivity trended with the oxygen percent (positive) and the carboxyl group fraction (negative). Of the two pressures, the lower pressure correlations had a lower standard error but also had more parameters to the fit. For the H_2S/CO_2 selectivities, three parameters correlated for both high and low pressures, the carbon percentage, oxygen percentage, and the carbonyl group fraction. Of these three parameters, the carbonyl group fraction had the greatest magnitude in slope. Finally, the CO_2/CH_4 selectivity had significant trends across all four experimental conditions with three parameters correlating across the experiments, the oxygen percent, the carboxyl group fraction, and the carbonyl group fraction. The oxygen percent had a negative correlation for all experiments (except the high-pressure PSA), the carboxyl group fraction correlated negatively for all experiments (except the high-pressure TSA), and the carbonyl group fraction correlated positively for all experiments (except the high-pressure PSA). Of the three parameters, the carbonyl group fraction had the greatest magnitude in slope.

Finally, the trends of adsorption and selectivity with the F_6-IPA adsorption were compared. This analysis showed that the H_2S/CO_2 selectivity was the only result that constantly showed a trend with the F_6-IPA adsorption. Interestingly, the selectivity trend is negative for the low-pressure experiment, but positive for the high-pressure experiments (Fig. 6). Note that H_2S is less acidic than CO_2.

3.2.2. Variable temperature studies

Experiments probing the temperature dependence of selectivity on the ACs were carried out by changing the adsorption temperature (T = 303 K, 333 K and 363 K) and the regeneration temperatures (T_{Regen} = 423 K, 623 K and 723 K) on the P_K and P_Na ACs. The P_K AC was chosen as pure component isotherms on this AC have been collected [7]; thus, the multi-component results can be modelled for this AC. The P_Na AC was chosen due to the early results at p = 2 bar showing it to be the most promising petcoke AC. The adsorption of CH_4, H_2S and CO_2 on the P_K and P_Na ACs for both TSA (T_{Regen} =723 K) and PSA experiments are reported in Fig. 7. The amounts adsorbed on the P_K AC for all three species decreased with increasing temperature, except for the CH_4 during the high-pressure PSA experiment. For the P_Na AC, the amount of CH_4 and CO_2 adsorbed for all experiments decreased with an increase in temperature. The amount of H_2S adsorbed on the P_Na AC did not show a trend with temperature for the TSA experiments. While the amount of H_2S adsorbed in the PSA experiments was observed to decrease with a temperature increase.

In Fig. 8, the selectivities H_2S/CH_4, H_2S/CO_2 and CO_2/CH_4 calculated from the adsorption results were compared to the selectivities estimated by the individual component adsorption trends in Fig. 9. For the TSA experiments (high and low pressure), the H_2S/CH_4 and and H_2S/CO_2 selectivities for both the P_K and P_Na ACs increased with adsorption temperature, indicating that a higher temperature would give a better separation of H_2S. The CO_2/CH_4 selectivities on the P_K AC were not significantly affected by temperature. Meanwhile, the P_Na AC was observed to have a decreasing selectivity for the high-pressure experiments, but not a significant trend with the low-pressure experiments. For the PSA experiments on the P_K AC, the H_2S selectivity over CH_4 and CO_2 and the CO_2/CH_4 selectivities decreased with higher temperatures. On the P_Na AC, the low-pressure H_2S selectivity over CH_4 and CO_2 increased with temperature, while the CO_2/CH_4 selectivity decreased. The high-pressure PSA experiments for the P_Na AC did not show significant trends for any of the three selectivities. The experimental selectivities for the P_K AC showed good agreement with the selectivities predicted by the linear fits of the adsorption data with a maximum reproducibility of 27% (high-pressure PSA H_2S/CH_4). The P_Na selectivity calculations also agreed with the experimental results; however, the percent errors were generally higher than the P_K calculations. The maximum error for the P_Na AC was 46% (high-pressure H_2S/CO_2). From these investigations into the temperature effects on the selectivities of the two ACs, it can be concluded that the P_Na AC would be better suited for higher temperature processes, with the increased H_2S selectivity over both CO_2 and CH_4.

The final temperature-dependent study investigated in this work was optimizing the regeneration temperature on the P_K and P_Na ACs (Fig. 9). These experiments were only conducted at p = 2 bar. From the adsorption trends for the two materials in Fig. 9**A**, it was observed that the adsorption capacity of CH_4 and CO_2 did not change significantly with the regeneration temperature of P_K. At the same time, P_Na experienced a decreasing capacity for CH_4 and CO_2 with increasing temperatures. Additionally, the H_2S capacity for both materials increased with the regeneration temperature. Of the two materials, the slope of the increase for H_2S was greater for P_Na than P_K.

In Fig. 9B, the experimental selectivities and the estimated selectivities are presented. From the comparison of the experimental data points and the estimated selectivities, a good agreement was observed for both materials. When the selectivities of the P_K AC were analyzed against regeneration temperature, an upward trend was observed for the H_2S/CH_4 (slope = 0.04 ± 0.01) and the H_2S/CO_2 (slope = 0.019 ± 0.004) selectivity, while the CO_2/CH_4 selectivity was insignificant (slope = -0.0004 ± 0.001). Similar findings were observed with the P_K AC, with an upward trend for the H_2S/CH_4 (slope = 0.3 ± 0.04) and the H_2S/CO_2 (slope = 0.1 ± 0.02) selectivities, and an insignificant result with regards to the CO_2/CH_4 selectivities (slope = -0.002 ± 0.004). By comparing how the selectivities changed with the regeneration temperature of the ACs, it was established that the H_2S selectivity of P_Na could be tuned by changing the regeneration temperature. At the same time, P_K demonstrated a weaker trend with the regeneration temperature. This interesting tuneability could be present in other ACs not tested here. Thus, investigating how the other ACs' adsorption and selectivities change with temperature could be the basis for future studies.

3.3. Multicomponent modelling

3.3.1. Pure component adsorption results

Pure component isotherms of CO_2, CH_4 and H_2S were collected for the P_K AC (Fig. 10) at three different temperatures (T = 288 K, 298 K and 308 K). The details of the experimental setup for the pure component adsorption measurements are provided in the SI of the manuscript. The pure component isotherms were fitted with the Langmuir isotherm equation, the parameters of which are found in Table 6. The Langmuir equation agrees with the experimental data collected as observed in the plots in Fig. 10 and the low mean sum squared error (MSSE) in Table 6. Isosteric heats of adsorption were calculated for CO_2, CH_4 and H_2S on P_K AC (Fig. 10, Table 7). A good agreement was observed when comparing the heats of adsorption calculated from the Langmuir equation to those determined by directly spline fitting raw data. The Langmuir capacities of the three fluids showed that H_2S and CO_2 had the same capacity (n^{∞} = 34 mmol g^{-1}), which was approximately double the capacity for CH_4 (n^{∞} = 16 mmol g^{-1}). Analysis of the isosteric heats of adsorp-

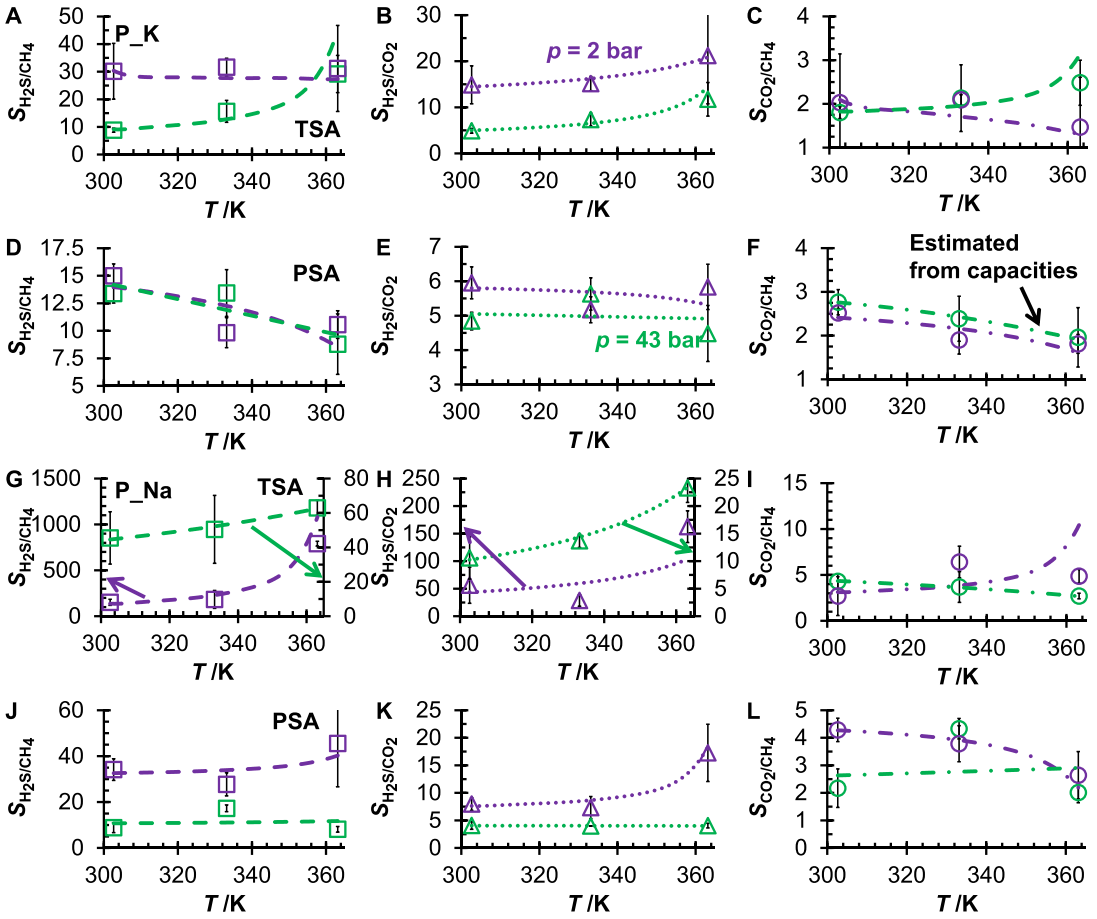

Fig. 8. The H_2S/CH_4 (□, ▬ ▬), H_2S/CO_2 (Δ, • •) and CO_2/CH_4 (○, ▬ •) selectivities on P_K (**A–F**) and P_Na (**G–L**) at various temperatures. The results for TSA (**A–C, G–I**)) and PSA (**C–D, J–L**) experiments at p = 2 bar (purple) and p = 43 bar (green) are reported. For all plots, the lines represent the predicted selectivity from the adsorption trends in Fig. 7.

Table 7
The Langmuir isotherm parameters for CO_2, CH_4 and H_2S on P_K AC.

Species	n^{∞}/mmol g^{-1}	b°/bar^{-1}	$\Delta_a H$/kJ mol^{-1}	MSSE /mmol g^{-1}
CO_2	33.97	7.06×10^{-6}	22.92	3.23×10^{-2}
CH_4	15.69	2.06×10^{-4}	14.69	1.72×10^{-2}
H_2S	33.97	1.66×10^{-6}	30.32	2.25×10^{-2}

tion showed that H_2S had the greatest heat of adsorption and CH_4had the lowest heat of adsorption. These trends agreed with the results obtained by de Oliviera et al. [23], where a coconut-husk AC was examined. However, in comparison, the P_K AC presented here demonstrated higher capacities for all three components and greater differences in the heats of adsorption than the coconut husk-AC. Adsorption of another component, water, was measured on P_K by TGA (Fig. S78). These results show that P_K has a very low affinity to water ($K_{H,298K}$ = 0.46 ± 0.03 mmol bar^{-1} g^{-1}). It is known that water adsorption is an essential consideration in natural gas applications as raw natural gas is saturated with water. Furthermore, the literature has established that water in simulated sour natural gas significantly reduces the selectivity of adsorbents such as zeolites and silica gels [65].

3.3.2. *Multicomponent modelling*

The multi-component adsorption results of the three models at p = 2 and 43 bar and T = 303 K, 333 K and 363 K were compared to the collected experimental results of P_K (Fig. S79). Compared to the experimental results, IAST fit better than CL (Fig. 11). However, it should be noted that IAST also had some limitations. For example, this model did not adequately predict the H_2S/CH_4 selectivity for the TSA experiments. Despite this, IAST still showed consistently lower error associated with selectivities than CL and thus was used for this work. For H_2S selectivities (H_2S/CH_4 and H_2S/CO_2), the results from IAST and CL were not much different, with IAST only having a slightly lower average residual than CL. Thus, even though CL is not the most accurate model, this simple model is applicable. The T = 303.15 K results for the IAST model are presented in Fig. S80 and for the CL model in Fig. S81.

Finally, using the IAST model, the H_2S selectivity of P_K was compared to the materials in Table 5 (Fig. 12). From these results, P_K was observed to have an H_2S/CO_2 selectivity that was competitive with the materials from the literature. One problem with using materials such as zeolites 4A, 5A and 13X is that they are sensitive to water in the system. The selectivity for other species drastically decreases due to water content [65]. This concern extends to some MOF species, such as MIL-101(Cr), where water interaction is comparable to some zeolites, as noted by the similar enthalpies of adsorption between the MOF and zeolites (Table 8), [66]. Materials displaying hydrophobic behaviour, such as ACs [67] and MOFs such as ZIF-8 [66], typically do not experience a drastic drop in the selectivity of adsorbed species in the presence of water.

Another important distinction between the activated carbons and inorganic materials, such as zeolites, are that activated carbons will be less selective based on molecule polarity and more selective based on polarizability, *i.e.*, dispersive interactions are dominant. This is evident with the H_2S/CH_4 selectivity being larger for the activated carbons, when

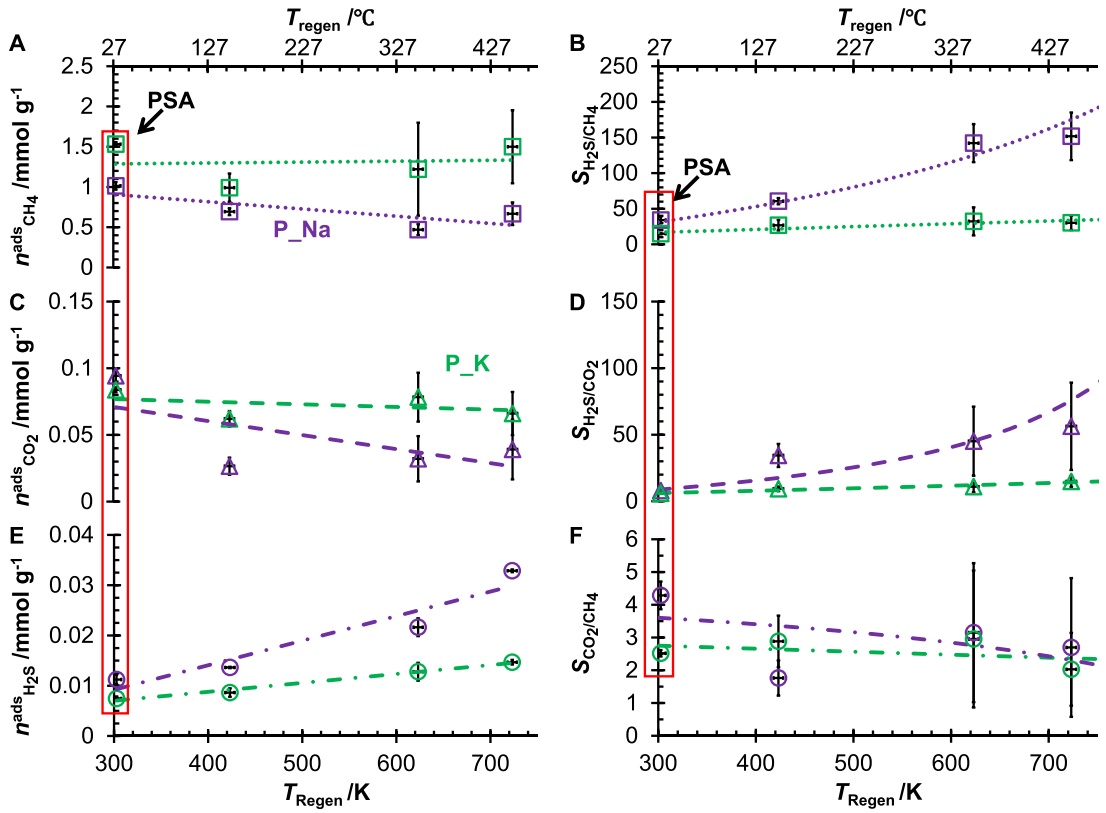

Fig. 9. The amount adsorbed at T = 303 K and p = 2 bar of CH_4 (□, • •), CO_2 (Δ, ▬ ▬) and H_2S (○, ▬ •) on the P_K (green) and P_Na (purple) ACs at various regeneration temperatures (A). The amount adsorbed of CH_4 (□, • •), CO_2 (Δ, ▬ ▬) and H_2S (○, ▬ •) on the P_K (green) and P_Na (purple) ACs, the lines indicate a linear fit (A, C, E). The H_2S/CH_4 (□, • •), H_2S/CO_2 (Δ, ▬ ▬) and CO_2/CH_4 (○, ▬ •) selectivities of the P_K (green) and P_Na (purple) ACs at various regeneration temperatures, the lines indicate predicted selectivity from the adsorption data trends (B, D, F).

Table 8
Isosteric enthalpies of adsorption of CO_2, CH_4 and H_2S on P_K AC.

Species	Spline fit $\Delta_a H$ /kJ mol^{-1}	Langmuir $\Delta_a H$ /kJ mol^{-1}	n^{ads} /mmol g^{-1}
CO_2	22.9 ± 2.0	22.9	4.0 – 19.0
CH_4	14.69 ± 0.02	14.76	4.0 – 9.5
H_2S	30.3 ± 0.7	30.3	5.0 – 23.0
H_2O	2.2 ± 0.9	3.8*	0.65 – 0.97**

Literature $\Delta_a H$ /kJ mol^{-1}

	Zeolite 4A[37]	Zeolite 13X[38]	MIL-101(Cr)[66]	ZIF-8[66]
H_2O	50.2	47.2	45.13	44.68

* Calculated from the Henry's law constants,
** μmol g^{-1}

compared to the zeolites in Fig. 12. Here H_2S has a very small polarity; however, the polarizability of H_2S is much greater than CH_4. The lack of polar interactions is also shown by the low water affinity of the activated carbons.

When comparing the heats of adsorption of zeolite 4A, 13X and MOFs MIL-101(Cr) and ZIF-8 from the literature with the P_K AC, it is evident that the heat of adsorption of water on the zeolites and MOFs are greater than the AC (Table 8). Interestingly, the heat of water adsorption on a known hydrophobic MOF, ZIF-8, was comparable to MIL-101(Cr), despite showing a Type V adsorption isotherm for water [66]. The isosteric heat of adsorption for water on the P_K AC is very low ($\Delta_a H$ = 3.8 kJ mol^{-1}) and agrees with the low experimental water adsorption determined (Fig. S78). The water adsorption isotherms of the other petcoke ACs tested herein are presented in Fig. S52 of the supporting information. The water uptake of the P_K AC was the lowest of the three ACs, but over all the ACs did not have a strong affinity for water. These results are not surprising as pristine graphitic surfaces do not show a strong affinity to water. Instead, water adsorption on carbon materials depends on surface functional group concentration [68]. Comparing the surface chemistry of P_K with that of P_K/st, P_Na and P_CK, there is no significant deviation in the concentration of functional groups.

3.4. COS formation catalysis

Through serendipity, it was observed that on three ACs (P_Na, P_CK and CB_CK), a peak for COS was present in the MS data (Fig. S81). It is well known that H_2S and CO_2 react to form some COS and water, and in these experiments, the concentration of COS in the feed gas was below the detectable limits of the GC analysis. Additionally, GEM calculations for the equilibrium concentrations in the gas feed showed that the COS concentration at T = 303.15 K would be 6 ppm. The water analysis during the experiments confirmed a water concentration of ~ 6 ppm_v during

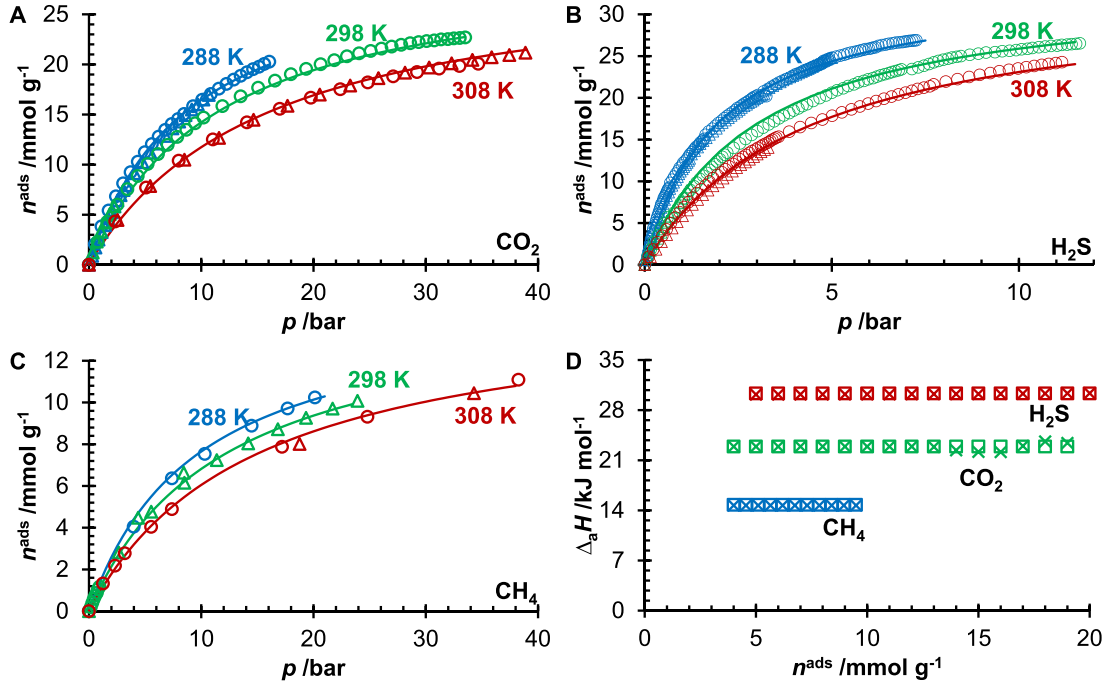

Fig. 10. Pure component absolute adsorption isotherms collected on the P_K AC. The symbols ○ and Δ denote separate experiments collected on the same thermally regenerated sample (**A, B, C**). Isotherms of CO_2 (**A**) were collected at T = 288.158 ± 0.005 K (blue ○), T = 288.154 ± 0.005 K (blue Δ), T = 298.155 ± 0.005 K (green ○), T = 298.156 ± 0.005 K (green Δ), T = 308.149 ± 0.005 K (red ○), T = 308.146 ± 0.005 K (red Δ). Isotherms of H_2S (**B**) were collected at T = 288.151 ± 0.005 K (blue ○), T = 288.153 ± 0.005 K (blue Δ), T = 298.157 ± 0.005 K (green ○), T = 298.156 ± 0.005 K (green Δ), T = 308.148 ± 0.005 K (red ○), T = 308.147 ± 0.005 K (red Δ). Isotherms of CH_4 (**C**) were collected at T = 288.150 ± 0.005 K (blue ○), T = 288.152 ± 0.005 K (blue Δ), T = 298.155 ± 0.005 K (green ○), T = 298.154 ± 0.005 K (green Δ), T = 308.156 ± 0.005 K (red ○), T = 308.146 ± 0.005 K (red Δ). The experimental results for T = 298 K were obtained from the literature [7]. The isosteric heats of adsorption vs. amount adsorbed for H_2S (red), CO_2 (green) and CH_4 (blue) on P_K AC (**D**). The symbols □ represent the heats of adsorption fit by the Langmuir isotherm equation and the and × the spline fit.

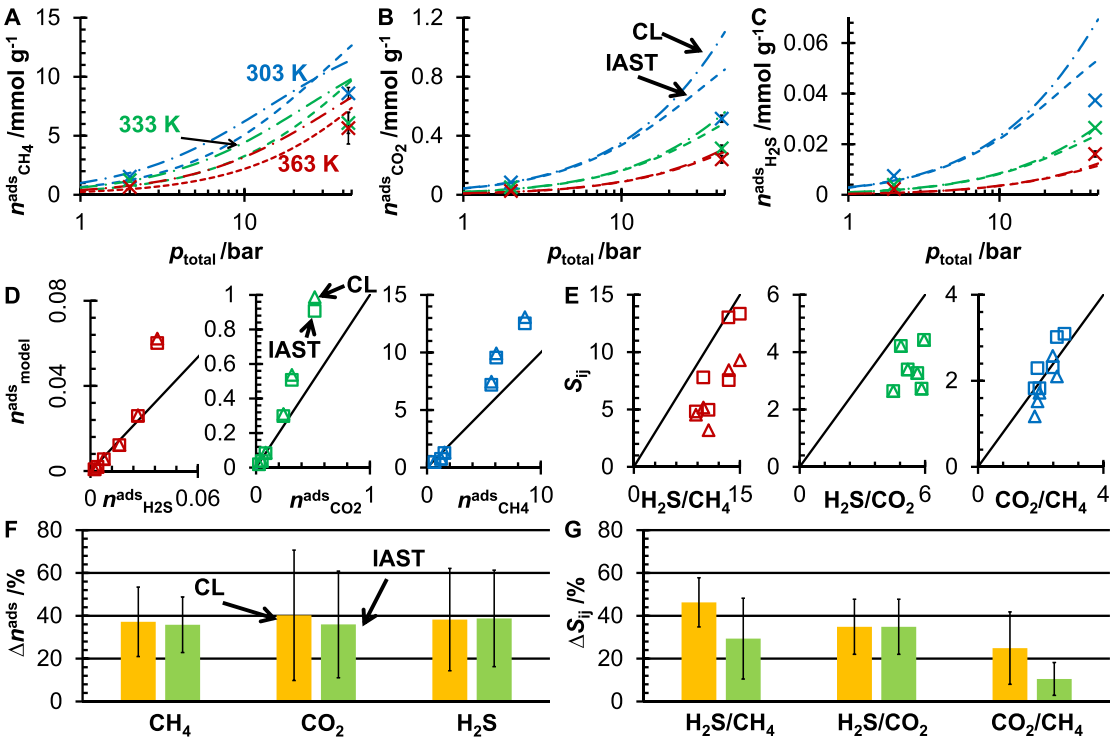

Fig. 11. Multi-component adsorption data (A, B, C), experimental data (×) and data predicted by CL (▬ •) and IAST (▬ ▬) at T = 303 K (blue), 333 K (green) and 363 K (red). Parity plots for amounts adsorbed of H_2S (red), CO_2 (green) and CH_4 (blue) (D) for CL (Δ) and IAST (□). Parity plots for H_2S/CH_4 (red), H_2S/CO_2 (green) and CO_2/CH_4 (blue) selectivities (E) for CL (Δ) and IAST (□). The average residuals for amount adsorbed (F) and selectivity (G) for CL (yellow) and IAST (green).

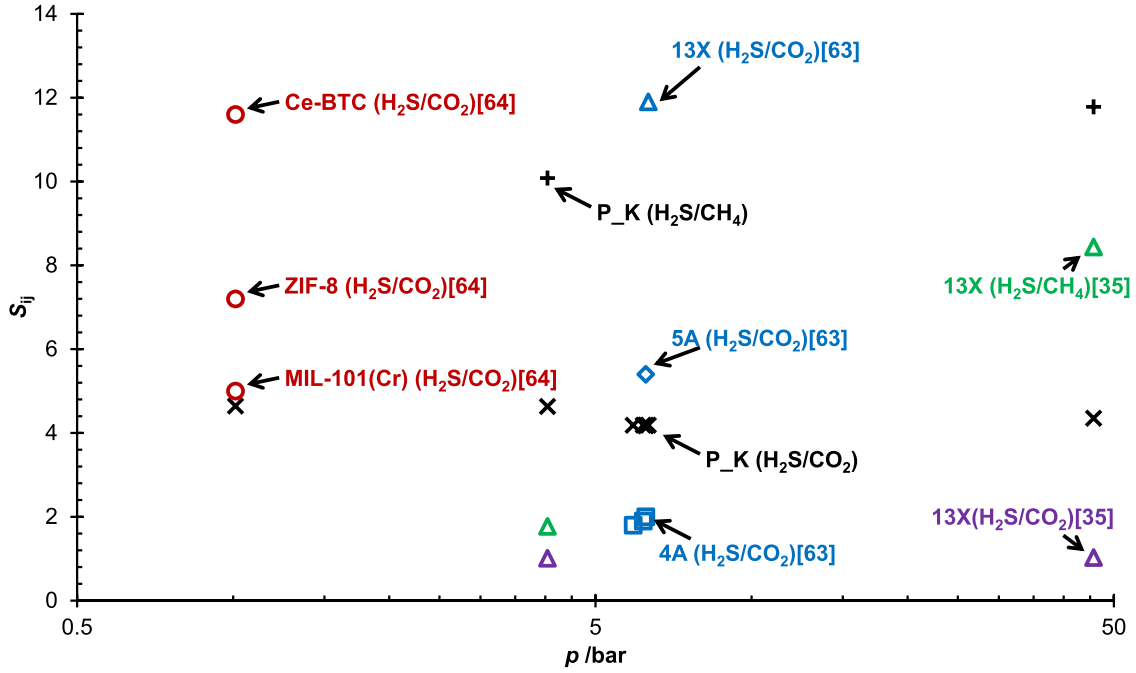

Fig. 12. The H_2S selectivities of various materials from the literature (values obtained from Table 5). The H_2S/CO_2 selectivity of zeolites 4A (blue, □) 5A (blue, ◊) and 13X (blue, Δ) from the work of Tomadakis *et al.* [59]; zeolite 13X (purple, Δ) from the work of Wynnyk [35]; MIL-101(Cr) (red, ○), ZIF-8 (red, ○) and Ce-BTC (red, ○) from the work of Liu et al. [60] and the IAST predictions for P_K (black, ×) at the same conditions as from the work from the literature. The H_2S/CH_4 selectivity for zeolite 13X (purple, Δ) from the work of Wynnyk [35] and the IAST predictions for P_K (black, +) at the same conditions as from the work from the literature.

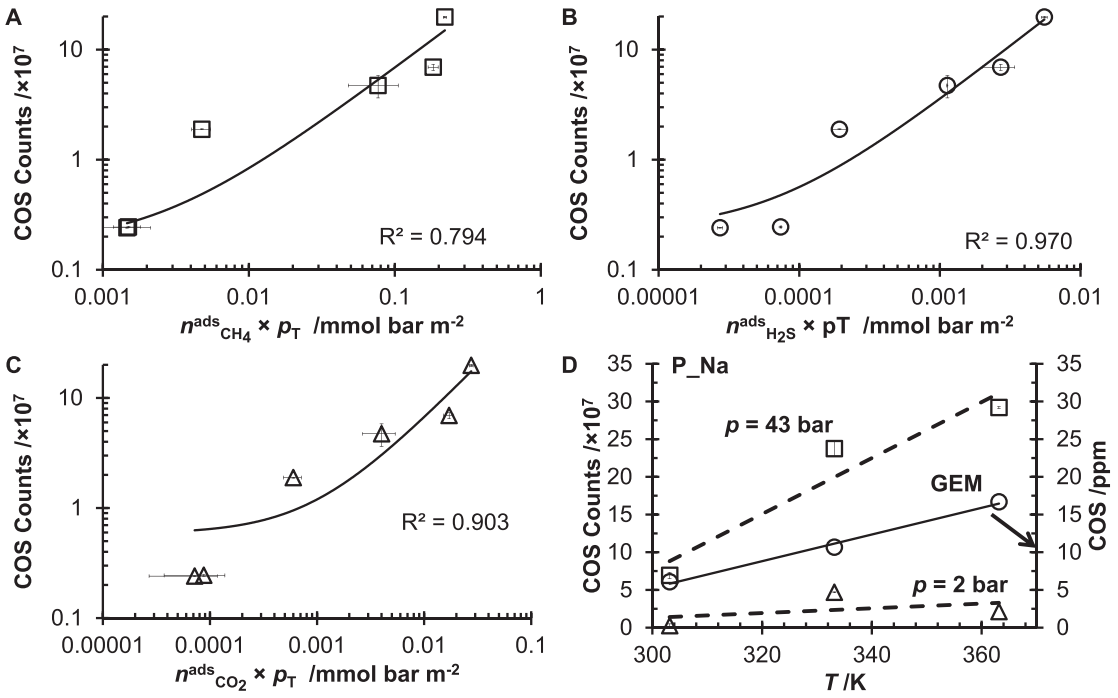

Fig. 13. The COS catalysis trends with the amount of CH_4 (A), CO_2 (B) and H_2S (C) adsorbed. The COS catalysis trends with temperature for P_Na and the GEM equilibrium COS concentration (D). The lines in these plots indicate linear fits.

the experiments. This concentration did not significantly change during the experiments, so it is difficult to track the COS production by following the water concentration. From the breakthrough data, for all three ACs, the COS counts increased concurrently with H_2S breakthrough and then decreased before H_2S plateaued.

The integrated COS peaks followed the same trend as the adsorption of the three ACs (Fig. 13). When the CH_4, H_2S, and CO_2 adsorption trends were investigated, the COS peak size appeared to correlate best with the H_2S and CO_2 adsorption, as expected for this reaction. For the P_Na AC, the COS production could be tracked over multiple temperatures (Fig. 13D). The production of COS increased with increasing

temperature, in line with the GEM calculations, which indicates that the equilibrium concentration of COS increased with temperature.

It should be noted that the investigation of the catalytic potential of these materials is limited; however, the hydrolysis (or reverse hydrolysis) is known to be base catalysed. In this case the surface basicity does not seem to correlate with the generation of COS. For example, Ecosorb and BPLC are more basic than P_Na or CB_CK, yet the COS generation was lower. It is most likely that the hydrolysis is in the diffusionally limited regime at these space velocities; therefore, a direct comparison of the chemical catalysis is not possible with this data. While this work focuses on the adsorption and separation of sour gas components on these ACs, the investigation into the H_2S/CO_2 catalysis for COS production on these materials remains for a future study under lower space velocities.

4. Conclusion

This work presented the characterization of 7 ACs, four derived from petroleum coke and three obtained commercially. The H_2S and CO_2 separation from a $CH_4/CO_2/H_2S$ mixture at $T = 303$ K, $p = 2$ bar and 43 bar were investigated by breakthrough experiments on the 7 ACs. Of the petcoke ACs, P_Na and P_CK were the most promising materials for H_2S and CO_2 separation, with maximum H_2S/CH_4 selectivities of 152 (P_Na, TSA) and 58 (P_CK, TSA) and CO_2/CH_4 selectivities of 4 (P_Na, TSA and PSA) and 4 (P_CK, PSA). Comparing the adsorption amount of CH_4, CO_2 and H_2S to the different material properties and compositions, CH_4 was proportional to the surface area, CO_2 was proportional to fraction of carbonyl and hydroxyl/ether groups, and H_2S was proportional to carbonyl groups fraction. Similar investigations into the selectivities demonstrated that H_2S/CH_4 selectivity was inversely proportional to the surface area, H_2S/CO_2 selectivity was proportional to the oxygen fraction of the ACs, and CO_2/CH_4 was inversely proportional to the fraction of carboxyl groups for the ACs. Further experiments for variable adsorption and regeneration temperatures on P_K and P_Na indicated that even at higher adsorption temperatures ($T = 363$ K), both materials remained selective for H_2S and CO_2 with the P_Na H_2S/CH_4 and H_2S/CO_2 selectivities even increasing at higher temperatures.

Pure component CH_4, CO_2 and H_2S isotherms were collected on the P_K AC and fit with the Langmuir isotherm equation. The pure component isotherms were used to calculate the multi-component adsorption using the CL and IAST models. The results of the multi-component models were compared with the experimental multi-component results for P_K, showing that CL and IAST had similar residuals for the selectivities. Using the IAST model, the H_2S selectivities with other adsorbents, MOFs and zeolites were compared at the same T and p conditions as the literature experiments. This comparison indicated that the P_K AC is competitive with these established adsorbents for separating H_2S from sour natural gas. Additionally, the low water affinity of the P_K AC means that H_2S selectivity would be retained in the presence of water.

From these experiments, it was demonstrated that petcoke ACs are viable candidates for H_2S and CO_2 separations. This is an important finding, as the materials are produced from a waste product that is currently abundant. Further studies into the adsorption and separation applications of the petcoke ACs are warranted, expressly, insight into the separation of flue gas and tail gas feeds. Future work will be required to determine the process parameters for optimal purification and regeneration. This could include regeneration upon partial bed loading and optimal space velocities to approach equilibrium.

Declaration of Competing Interest

The authors declare no competing financial interest.

CRediT authorship contribution statement

John H. Jacobs: Validation, Formal analysis, Investigation, Writing – original draft, Writing – review & editing, Visualization. **Nancy Chou:** Methodology, Validation, Investigation, Writing – review & editing. **Kaylan H. McKelvie:** Investigation, Writing – review & editing. **Jerry A. Commodore:** Investigation, Writing – review & editing. **Ruohong Sui:** Methodology, Validation, Writing – review & editing. **Kevin L. Lesage:** Methodology, Validation, Writing – review & editing. **Kyle G. Wynnyk:** Methodology, Validation, Writing – review & editing. **Ye Xiao:** Resources, Writing – review & editing. **Mark C. Biesinger:** Methodology, Writing – review & editing. **Josephine M. Hill:** Resources, Writing – review & editing, Supervision, Funding acquisition. **Robert A. Marriott:** Conceptualization, Methodology, Writing – review & editing, Supervision, Funding acquisition, Resources.

Data availability

Data will be made available on request.

Acknowledgement

The funding for this research was provided through the Natural Science and Engineering Research Council of Canada (NSERC) and Alberta Sulphur Research Ltd. (ASRL) Industrial Research Chair in Applied Sulfur Chemistry. In addition to NSERC, the authors are grateful to the sponsoring member companies of ASRL.

Supplementary materials

Supplementary material associated with this article can be found, in the online version, at doi:10.1016/j.cartre.2022.100243.

References

[1] R.A. Marriott, P. Pirzadeh, J. Marrugo-Hernandez, S. Raval, Hydrogen sulfide formation in oil and gas, Can. J. Chem. 94 (2016) 406–413, doi:10.1139/cjc-2015-0425.
[2] K.I. Adeniyi, H.H. Wan, C.E. Deering, F. Bernard, M.A. Chisholm, R.A. Marriott, High-pressure hydrogen sulfide experiments: how did our safety measures and hazard control work during a failure event? Safety 6 (2020) 15, doi:10.1016/j.fluid.2020.112865.
[3] R. Ciccoli, V. Cigolotti, R. Lo Presti, E. Massi, S.J. McPhail, G. Monteleone, A. Moreno, V. Naticchioni, C. Paoletti, E. Simonetti, F. Zaza, Molten carbonate fuel cells fed with biogas: combating H_2S, Waste Manag. 30 (2010) 1018–1024, doi:10.1016/j.wasman.2010.02.022.
[4] V. Cigolotti, Ph.D, University of Naples Federico II, 2009.
[5] G.E. Likens, F.H. Bormann, Acid rain: a serious regional environmental problem, Science 184 (1974) 1176–1179, doi:10.1126/science.184.4142.1176.
[6] N.R. Glass, D.E. Arnold, J.N. Galloway, G.R. Hendrey, J.J. Lee, W.W. McFee, S.A. Norton, C.F. Powers, D.L. Rambo, C.L. Schofield, Effects of acid precipitation, Environ. Sci. Technol. 16 (1982) 162A–169A.
[7] J.H. Jacobs, K.G. Wynnyk, R. Lalani, R. Sui, J. Wu, V. Montes, J.M. Hill, R.A. Marriott, Removal of sulfur compounds from industrial emission using activated carbon derived from petroleum coke, Ind. Eng. Chem. Res. 58 (2019) 18896–18900, doi:10.1021/acs.iecr.9b04443.
[8] M.S. Shah, M. Tsapatsis, J.I. Siepmann, Hydrogen sulfide capture: from absorption in polar liquids to oxide, zeolite, and metal–organic framework adsorbents and membranes, Chem. Rev. 117 (2017) 9755–9803, doi:10.1021/acs.chemrev.7b00095.
[9] P.K. Koech, J.E. Rainbolt, M.D. Bearden, F. Zheng, D.J. Heldebrant, Chemically selective gas sweetening without thermal-swing regeneration, Energy Environ. Sci. 4 (2011) 1385, doi:10.1039/C0EE00839G.
[10] M. Khabazipour, M. Anbia, Removal of hydrogen sulfide from gas streams using porous materials: a review, Ind. Eng. Chem. Res. 58 (2019) 22133–22164, doi:10.1021/acs.iecr.9b03800.
[11] A. Georgiadis, N. Charisiou, M. Goula, Removal of hydrogen sulfide from various industrial gases: a review of the most promising adsorbing materials, Catalysts 10 (2020) 521, doi:10.3390/catal10050521.
[12] C. Halliday, T.A. Hatton, Sorbents for the capture of CO_2 and other acid gases: a review, Ind. Eng. Chem. Res. 60 (2021) 9313–9346, doi:10.1021/acs.iecr.1c00597.
[13] R. Sitthikhankaew, D. Chadwick, S. Assabumrungrat, N. Laosiripojana, Effects of humidity, O_2, and CO_2 on H_2S adsorption onto upgraded and KOH impregnated activated carbons, Fuel Process. Technol. 124 (2014) 249–257, doi:10.1016/j.fuproc.2014.03.010.
[14] N.N. Zulkefli, M.S. Masdar, W.N.R. Wan Isahak, J. Md Jahim, S.A. Md Rejab, C. Chien Lye, Removal of hydrogen sulfide from a biogas mimic by using impregnated activated carbon adsorbent, PLoS ONE 14 (2019) e0211713, doi:10.1371/journal.pone.0211713.
[15] J. Wu, V. Montes, L.D. Virla, J.M. Hill, Impacts of amount of chemical agent and addition of steam for activation of petroleum coke with KOH or NaOH, Fuel Process. Technol. 181 (2018) 53–60, doi:10.1016/j.fuproc.2018.09.018.

[16] L.D. Virla, V. Montes, J. Wu, S.F. Ketep, J.M. Hill, Synthesis of porous carbon from petroleum coke using steam, potassium and sodium: combining treatments to create mesoporosity, Microporous Mesoporous Mater. 234 (2016) 239–247, doi:10.1016/j.micromeso.2016.07.022.

[17] V. Montes, J.M. Hill, Activated carbon production: recycling KOH to minimize waste, Mater. Lett. 220 (2018) 238–240, doi:10.1016/j.matlet.2018.03.019.

[18] G.G. Stavropoulos, A.A. Zabaniotou, Minimizing activated carbons production cost, Fuel Process. Technol. 90 (2009) 952–957, doi:10.1016/j.fuproc.2009.04.002.

[19] X. Li, J. Chen, Adsorption of natural gas and its whole components on adsorbents, Adsorption 17 (2011) 949–954, doi:10.1007/s10450-011-9373-z.

[20] T. Mochizuki, M. Kubota, H. Matsuda, L.F. D'Elia Camacho, Adsorption behaviors of ammonia and hydrogen sulfide on activated carbon prepared from petroleum coke by KOH chemical activation, Fuel Process. Technol. 144 (2016) 164–169, doi:10.1016/j.fuproc.2015.12.012.

[21] K.S. Walton, D.S. Sholl, Predicting multicomponent adsorption: 50 years of the ideal adsorbed solution theory, AIChE J. 61 (2015) 2757–2762, doi:10.1002/aic.14878.

[22] D.D. Do, Adsorption Analysis: Equilibria and Kinetics, Imperial College Press, London, 1998.

[23] L.H. de Oliveira, J.G. Meneguin, M.V. Pereira, J.F. do Nascimento, P.A. Arroyo, Adsorption of hydrogen sulfide, carbon dioxide, methane, and their mixtures on activated carbon, Chem. Eng. Commun. 206 (2019) 1533–1553, doi:10.1080/00986445.2019.1601627.

[24] E.C. Markham, A.F. Benton, The adsorption of gas mixtures by silica, J. Am. Chem. Soc. 53 (1931) 497–507, doi:10.1021/ja01353a013.

[25] R. Bai, R.T. Yang, A thermodynamically consistent langmuir model for mixed gas adsorption, J. Colloid Interface Sci. 239 (2001) 296–302, doi:10.1006/jcis.2001.7563.

[26] A.L. Myers, J.M. Prausnitz, Thermodynamics of mixed-gas adsorption, AIChE J. 11 (1965) 121–127, doi:10.1002/aic.690110125.

[27] S. Brunauer, P.H. Emmett, E. Teller, Adsorption of gases in multimolecular layers, J. Am. Chem. Soc. 60 (1938) 309–319, doi:10.1021/ja01269a023.

[28] E. Ep. Barrett, L.G. Joyner, P.P Halenda, The determination of pore volume and area distributions in porous substances. I. Computations from nitrogen isotherms, J. Am. Chem. Soc. 73 (1951) 373–380, doi:10.1021/ja01145a126.

[29] B. Lippens, Studies on pore systems in catalysts V. The t method, J. Catal. 4 (1965) 319–323, doi:10.1016/0021-9517(65)90307-6.

[30] M.M. Dubinin, Adsorption in micropores, J. Colloid Interface Sci. 23 (1967) 487–499, doi:10.1016/0021-9797(67)90195-6.

[31] M.C. Biesinger, Accessing the robustness of adventitious carbon for charge referencing (Correction) purposes in XPS analysis: insights from a multi-user facility data review, Appl. Surf. Sci. 597 (2022) 153681, doi:10.1016/j.apsusc.2022.153681.

[32] D.J. Morgan, Comment on the XPS analysis of carbon materials, J. Carbon. Res. 7 (2021) 51, doi:10.3390/c7030051.

[33] B. Moeini, M.R. Linford, N. Fairley, A. Barlow, P. Cumpson, D. Morgan, V. Fernandez, J. Baltrusaitis, Definition of a new (Doniach-Sunjic-Shirley) peak shape for fitting asymmetric signals applied to reduced graphene oxide/graphene oxide XPS spectra, Surf. Interface Anal. 54 (2022) 67, doi:10.1002/sia.7021.

[34] T.R. Gengenbach, G.H. Major, M.R. Linford, C.D. Easton, Practical guides for X-ray photoelectron spectroscopy (XPS): Interpreting the carbon 1s spectrum, J. Vac. Sci. Technol. A 39 (2021) 013204, doi:10.1116/6.0000682.

[35] K.G. Wynnyk, Ph.D, University of Calgary, 2019.

[36] K.G. Wynnyk, B. Hojjati, P. Pirzadeh, R.A. Marriott, High-pressure sour gas adsorption on zeolite 4A, Adsorption 23 (2017) 149–162, doi:10.1007/s10450-016-9841-6.

[37] K.G. Wynnyk, B. Hojjati, R.A. Marriott, High-pressure sour gas and water adsorption on zeolite 13X, Ind. Eng. Chem. Res. 57 (2018) 15357–15365, doi:10.1021/acs.iecr.8b03317.

[38] K.G. Wynnyk, B. Hojjati, R.A. Marriott, Sour gas and water adsorption on common high-pressure desiccant materials: Zeolite 3A, Zeolite 4A, and silica gel, J. Chem. Eng. Data 64 (2019) 3156–3163, doi:10.1021/acs.jced.9b00233.

[39] J.H. Jacobs, C.E. Deering, K.L. Lesage, M.J. Stashick, R.A. Marriott, Rapid cycling thermal swing adsorption apparatus: commissioning and data analyses for water adsorption of zeolites 4A and 13X Over 2000 cycles, Ind. Eng. Chem. Res. 60 (2021) 7487–7494, doi:10.1021/acs.iecr.1c00469.

[40] R. Span, W. Wagner, A new equation of state for carbon dioxide covering the fluid region from the triple-point temperature to 1100 K at pressures up to 800 MPa, J. Phys. Chem. Ref. Data 25 (1996) 1509–1596, doi:10.1063/1.555991.

[41] U. Setzmann, W. Wagner, A new equation of state and tables of thermodynamic properties for methane covering the range from the melting line to 625 K at pressures up to 100 MPa, J. Phys. Chem. Ref. Data 20 (1991) 1061–1155, doi:10.1063/1.555898.

[42] E.W. Lemmon, R. Span, Short fundamental equations of state for 20 industrial fluids, J. Chem. Eng. Data 51 (2006) 785–850, doi:10.1021/je050186n.

[43] W. Wagner, A. Pruß, The IAPWS formulation 1995 for the thermodynamic properties of ordinary water substance for general and scientific use, J. Phys. Chem. Ref. Data 31 (2002) 387–535, doi:10.1063/1.1461829.

[44] D.O. Ortiz Vega, Ph.D, Texas A & M University, 2013.

[45] E.W. Lemmon, I.H. Bell, M.L. Hubaer, M.O. McLinden, NIST. Reference Fluid Thermodynamics and Transport Properties - REFPROP, National Institute of Standards and Technology, Gaithersburg, 2013.

[46] O. Kunz, W. Wagner, The GERG-2008 wide-range equation of state for natural gases and other mixtures: an expansion of GERG-2004, J. Chem. Eng. Data 57 (2012) 3032–3091, doi:10.1021/je300655b.

[47] S. Sircar, Measurement of gibbsian surface excess, AIChE J. 47 (2001) 1169–1176, doi:10.1002/aic.690470522.

[48] A.V. Neimark, P.I. Ravikovitch, Calibration of pore volume in adsorption experiments and theoretical models, Langmuir 13 (1997) 5148–5160, doi:10.1021/la970266s.

[49] A.L. Myers, P.A. Monson, Physical adsorption of gases: the case for absolute adsorption as the basis for thermodynamic analysis, Adsorption 20 (2014) 591–622, doi:10.1007/s10450-014-9604-1.

[50] K. Murata, J. Miyawaki, K. Kaneko, A simple determination method of the absolute adsorbed amount for high pressure gas adsorption, Carbon 40 (2002) 425–428, doi:10.1016/S0008-6223(01)00126-9.

[51] I. Langmuir, The adsorption of gases on plane surfaces of glass, mica and platinum, J. Am. Chem. Soc. 40 (1918) 1361–1403, doi:10.1021/ja02242a004.

[52] E. Hückel, Theory of heat evolved in capillary condensation, Trans. Farad. Soc. 28 (1932) 382–386, doi:10.1039/TF9322800382.

[53] R. Defay, I. Prigogine, A. Bellemans, D. Everett, Surface Tension and Adsorption, Longmans, London, 1966.

[54] C.E. Deering, M.J. Saunders, J.A. Commodore, R.A. Marriott, The volumetric properties of carbonyl sulfide and carbon dioxide mixtures from T = 322 to 393 K and p = 2.5 to 35 MPa: application to COS hydrolysis in subsurface injectate streams, J. Chem. Eng. Data 61 (2016) 1341–1347, doi:10.1021/acs.jced.5b01061.

[55] J.A. Commodore, C.E. Deering, F. Bernard, R.A. Marriott, High-pressure densities and excess molar volumes for the binary mixture of carbon dioxide and hydrogen sulfide at T = 343–397 K, J. Chem. Eng. Data (2021) acs.jced.1c00446, doi:10.1021/acs.jced.1c00446.

[56] J.A. Commodore, Ph.D, University of Calgary, 2021.

[57] M. Chase, NIST-JANAF Thermochemical Tables, American Institute of Physics, 4th Ed.

[58] R. Sui, C.B. Lavery, C.E. Deering, R. Prinsloo, D. Li, N. Chou, K.L. Lesage, R.A. Marriott, Improved carbon disulfide conversion: modification of an alumina Claus catalyst by deposition of transition metal oxides, Appl. Catal. A Gener. 604 (2020) 117773, doi:10.1016/j.apcata.2020.117773.

[59] M.M. Tomadakis, H.H. Heck, M.E. Jubran, K. Al-Harthi, Pressure-swing adsorption separation of H_2S fromCO_2 with molecular sieves 4A, 5A, and 13X, Sep. Sci. Technol. 46 (2011) 428–433, doi:10.1080/01496395.2010.520292.

[60] J. Liu, Y. Wei, P. Li, Y. Zhao, R. Zou, Selective H_2S/CO_2 separation by metal–organic frameworks based on chemical-physical adsorption, J. Phys. Chem. C 121 (2017) 13249–13255, doi:10.1021/acs.jpcc.7b04465.

[61] J.P. Boudou, M. Chehimi, E. Broniek, T. Siemieniewska, J. Bimer, Adsorption of H_2S or SO_2 on an activated carbon cloth modified by ammonia treatment, Carbon 41 (2003) 1999–2007, doi:10.1016/S0008-6223(03)00210-0.

[62] L. Hamon, C. Serre, T. Devic, T. Loiseau, F. Millange, G. Férey, G. De Weireld, Comparitive study of hydrogen sulfide adsorption in the MIL-53(Al, Cr, Fe), MIL-47(V), MIL-100(Cr), and MIL-101(Cr), J. Am. Chem. Soc. 131 (2009) 8775–8777, doi:10.1021/ja901587t.

[63] F. Shen, J. Liu, C. Gu, D. Wu, Roles of oxygen functional groups in hydrogen sulfide adsorption on activated carbon surface: a density functional study, Ind. Eng. Chem. Res. 58 (2019) 5526–5532, doi:10.1021/acs.iecr.9b00507.

[64] X. Song, L. Wang, J. Gong, X. Zhan, Y. Zeng, Exploring a new method to study the effects of surface functional groups on adsorption of CO_2 and CH_4 on activated carbons, Langmuir 36 (2020) 3862–3870, doi:10.1021/acs.langmuir.9b03475.

[65] B. Steuten, C. Pasel, M. Luckas, D. Bathen, Trace level adsorption of toxic sulfur compounds, carbon dioxide, and water from methane, J. Chem. Eng. Data 58 (2013) 2465–2473, doi:10.1021/je400298r.

[66] P. Küsgens, M. Rose, I. Senkovska, H. Fröde, A. Henschel, S. Siegle, S. Kaskel, Characterization of metal-organic frameworks by water adsorption, Microporous Mesoporous Mater. 120 (2009) 325–330, doi:10.1016/j.micromeso.2008.11.020.

[67] J.K. Brennan, T.J. Bandosz, K.T. Thomson, K.E. Gubbins, Water in porous carbons, Colloids Surf. A Physicochem. Eng. Asp. 187–188 (2001) 539–568, doi:10.1016/S0927-7757(01)00644-6.

[68] S.J. Tan, D.D. Do, J.W. Chew, The physisorption mechanism of SO_2 on graphitized carbon, Phys. Chem. Chem. Phys. 22 (2020) 21463–21473, doi:10.1039/D0CP03860A.